Title

Active flexural-slip faulting: A study from the Pamir-Tian Shan convergent zone, NW China

Journal

Journal of Geophysical Research: Solid Earth, 120(6)

ISSN

2169-9313

Authors

Li, Tao

Chen, Jie

Thompson, Jessica A

et al.

Publication Date

2015-06-01

DOI

10.1002/2014jb011632

Peer reviewed

AGU PUBLICATIONS

JGR

Journal of Geophysical Research: Solid Earth

RESEARCH ARTICLE
10.1002/2014JB011632

Key Points:
- FSF scarps occur near synclinal hinges, play important roles in folding process
- FSF scarp height and land surface's tilt angle have predictable geometry
- Active FSFs can be used to determine seismic hazards related with blind thrusts

Supporting Information:
- Table S1 caption
- Table S1

Correspondence to:
T. Li,
litao.410@163.com

Citation:
Li, T., J. Chen, J. A. Thompson, D. W. Burbank, and X. Yang (2015), Active flexural-slip faulting: A study from the Pamir-Tian Shan convergent zone, NW China, *J. Geophys. Res. Solid Earth*, *120*, 4359–4378, doi:10.1002/2014JB011632.

Received 23 SEP 2014
Accepted 1 MAY 2015
Accepted article online 5 MAY 2015
Published online 3 JUN 2015

Active flexural-slip faulting: A study from the Pamir-Tian Shan convergent zone, NW China

Tao Li[1,2], Jie Chen[1], Jessica A. Thompson[3,4], Douglas W. Burbank[3], and Xiaodong Yang[1,5]

[1]State Key Laboratory of Earthquake Dynamics, Institute of Geology, China Earthquake Administration, Beijing, China, [2]Research Institute of Petroleum Exploration and Development, Petro China, Beijing, China, [3]Department of Earth Science, University of California, Santa Barbara, California, USA, [4]Now at ConocoPhillips, Houston, Texas, USA, [5]The Second Monitoring and Application Center, China Earthquake Administration, Xi'an, China

Abstract The flexural-slip fault (FSF), a type of secondary fault generated by bed-parallel slip, occurs commonly and plays an important role in accommodating fold growth. Although the kinematics and mechanics of FSFs are well studied, relatively few field observations or geometric models explore its geomorphic expression. In the Pamir-Tian Shan convergent zone, NW China, suites of well-preserved FSF scarps displace fluvial terraces in the Mingyaole and Wulagen folds. Integrating interpretations of Google Earth images, detailed geologic and geomorphic mapping, and differential GPS measurements of terrace surfaces, we summarize geomorphic features that typify these faults and create kinematic models of active flexural-slip faulting. Our study indicates the following: (i) FSF scarps commonly occur near synclinal hinges, irrespective of whether (a) the dip direction of beds on either side of the hinge is unidirectional or in opposite directions, (b) the hinge is migrating or fixed, or (c) the hinge shape is narrow and angular or wide and curved. (ii) Active FSFs are likely to produce higher scarps on steeper beds, whereas lower or no topographic scarps typify gentler beds. (iii) Tilt angles of the terrace surface displaced above FSFs progressively decrease farther away from the hinge, with abrupt changes in slope coinciding with FSF scarps; the changes in tilt angle and scarp height have a predictable geometric relationship. (iv) Active FSFs can accommodate a significant fraction of total slip and play a significant role in folding deformation. (v) Active FSFs may be used to assess seismic hazards associated with active folds and associated blind thrusts.

1. Introduction

During the development of folds, bed-parallel slip along weak beds can produce flexural-slip faults (FSFs): a common class of secondary faults (Figure 1). Such faults are typically present in a sequence of relatively competent beds alternating with thin incompetent beds [*Ramsay*, 1967; *Tanner*, 1989; *Yeats et al*., 1997; *Ismat and Mitra*, 2005a, 2005b]. As folding proceeds, the faults are progressively activated from one potential slip surface to another and their spacing decreases [*Tanner*, 1989; *Johnson and Johnson*, 2000]. FSFs are unrooted and vanish at depth (Figure 1), and the amount of slip along the fault, which is a function of bed dip and thickness, decreases to zero at the fold hinge [*Ramsay*, 1967; *Yeats et al*., 1981, 1997; *Johnson and Johnson*., 2000; *Sanz et al*., 2008].

Because FSFs do not produce stratigraphic separation, they are difficult to recognize in bedrock outcrops or seismic reflection data. However, if the bedrock has been beveled by young geomorphic surfaces, e.g., terrace surfaces or alluvial fans (Figure 1), FSFs can displace the land surface to produce an array of subparallel geomorphic scarps. In particular, in arid settings where little vegetation obscures the surface, even subtle FSF scarps can be well preserved and readily discernible. Although the kinematics and mechanics of FSFs are well studied, relatively few field observations and geometric models have described their geomorphic expression. *Yeats et al*. [1981, 1997] demonstrated that the hanging wall and footwall of a FSF lie on the side of the synclinal hinge and anticlinal hinge, respectively. Accordingly, the fault shows reverse separation where the subjacent bed is upright and normal separation where the bed is overturned. The land surface overlying a FSF is likely to be tilted toward the synclinal hinge (Figure 1) and in the same direction as underlying folded beds [*Yeats et al*., 1981, 1997; *Rockwell et al*., 1984; *Burbank and Anderson*, 2011; *Li et al*., 2011, 2014; T. Li et al., Hinge-migrated fold scarp model based on analysis of bed geometry: A study from the Mingyaole anticline, southern foreland of Chinese Tian Shan, *Journal of Geophysical Research*: *Solid Earth*, under review, 2015]. FSFs may slip at high rates (>1 mm/a) and accommodate considerable deformation during folding [*Rockwell et al*., 1984].

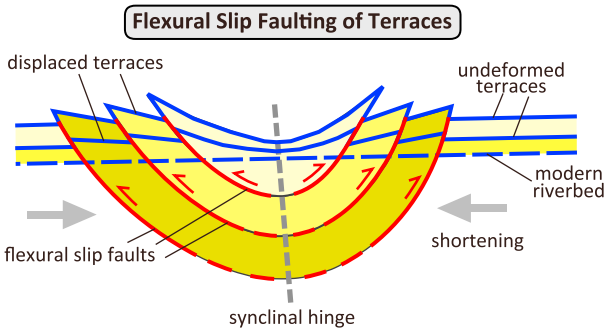

Figure 1. Active flexural-slip faulting model. Slip along the fault plane decreases to zero at the fold hinge. Terrace surfaces on the hanging wall of FSFs are tilted in the same directions as the dip of underlying beds. Modified from *Burbank and Anderson* [2011].

Yeats et al. [1981, 1997] proposed that FSFs have low potential for creating large, destructive earthquakes but may represent an independent source of low-magnitude earthquakes [*Shaw and Suppe*, 1994; *Kelsey et al.*, 2008]. FSFs may rupture coseismically with a master fault [*Philip and Meghraoui*, 1983; *Klinger and Rockwell*, 1989; *Walker et al.*, 2003, 2013; *Ishiyama et al.*, 2004; *Berberian*, 2014; *Gutiérrez et al.*, 2014] and can influence the upward propagation of a seismogenic master fault and development of the associated fold geometry [*Roering et al.*, 1997; *Niño et al.*, 1998; *Mitra*, 2002]. A recent study [*Gutiérrez et al.*, 2014] indicates that coseismic deposits preserved by FSFs can record paleo-earthquake history of the master fault. These characteristics imply the importance and necessity of considering active FSFs in the study of active folding.

In NW China, numerous active folds are present within the Pamir-Tian Shan convergent zone (Figure 2). In field surveys of this area, a series of strikingly clear FSF scarps are well preserved on terrace surfaces that have been incised into the Mingyaole and Wulagen folds. Based on the interpretation of Google Earth images, detailed geologic and geomorphic mapping, differential GPS topographic measurements, and published ages of terrace surfaces, we conducted a thorough investigation of active FSFs, including an analysis of the relationship between FSF scarps and characteristics of the fold hinge. We summarized key deformation patterns of active flexural-slip faulting of terrace surfaces and created kinematic and geomorphic models of FSFs. Finally, we discussed the implications of FSFs for seismic risk and the detection of active folds and associated blind thrusts.

2. Tectonic Setting

The Pamir, a northward convex mountain range, lies in the northwestern syntaxis of the Indo-Asian collision system. Since about 25–20 Ma [*Sobel and Dumitru*, 1997; *Yin et al.*, 2002], the northern Pamir has indented northward ~300 km [*Burtman and Molnar*, 1993], an indentation accommodated by the following: (i) south

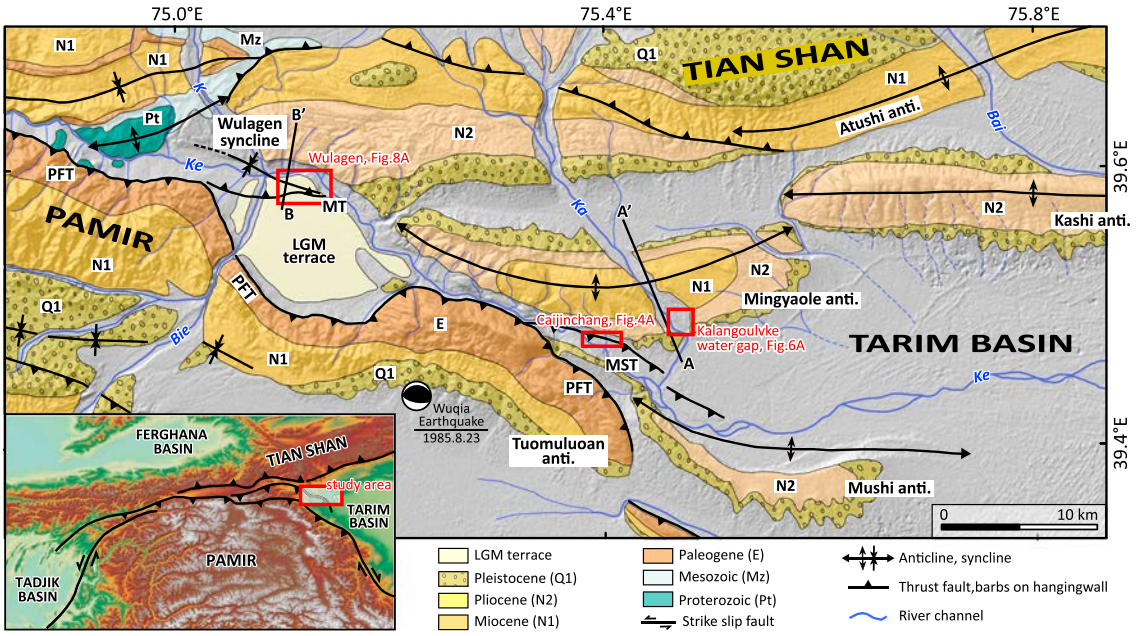

Figure 2. Geologic map of the Pamir-Tian Shan convergent zone, NW China. Inset shows the simplified tectonic setting and topography of the study area. Bai: Baishikeremu River, Bie: Biertuokuoyi River, K: Kangsu River, Ka: Kalangoulvke River, Ke: Kezilesu River, MST: Mingyaole South Thrust, MT: Mayikake Thrust, and PFT: Pamir Frontal Thrust.

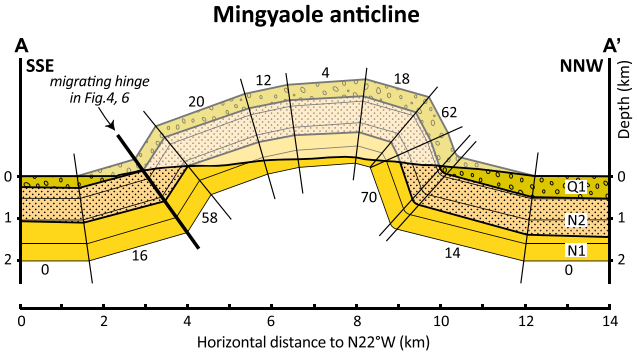

Figure 3. Geologic cross section of the Mingyaole fold (see Figure 2 for location). Above the modern topography, the bed colors are lighter. Modified from *Scharer et al.* [2006] and T. Li et al. (under review, 2015).

dipping intracontinental subduction, as outlined by intermediate-depth seismicity along the northern Pamir margin [*Burtman and Molnar*, 1993; *Arrowsmith and Strecker*., 1999; *Negredo et al*., 2007; *Schneider et al*., 2013; *Sippl et al*., 2013]; (ii) sinistral strike-slip faulting on its western margin; and (iii) dextral strike-slip faulting on its eastern margin (Figure 2 inset) [*Burtman and Molnar*, 1993]. In response to the indentation, structures along the southern margin of the Tian Shan were reactivated around 25–18 Ma [*Yin et al*., 1998; *Sobel et al*., 2006], and deformation then episodically migrated southward to produce a series of subparallel fold belts (Figure 2) [*Chen et al*., 2002, 2007a; *Scharer et al*., 2004, 2006; *Heermance et al*., 2008].

Situated between the Pamir and Tian Shan and accompanying uplift of these two ranges, the western Tarim Basin has subsided significantly and has been filled by an 8 to 12 km thick, coarsening upward sequence that tapers toward the basin interior from the surrounding range fronts [*Wei et al*., 2013]. During this time, the basin has transitioned gradually from marine to continental deposition [*Bosboom et al*., 2010], has been disrupted by forelandward propagation of thrust systems [*Wei et al*., 2013], and has been rotated clockwise due to compression along its irregular boundaries [*Reigber et al*., 2001].

Since late Miocene-Pliocene times, deformation along the eastern margin of the Pamir ceased [*Cowgill*, 2010; *Sobel et al*., 2011, 2013], and the Pamir welded together with the Tarim Basin to collide with the Tian Shan. This tectonic transformation has caused deformation to transfer from both the Pamir's eastern margin and its northwestern extension to the Pamir-Tian Shan convergent zone, which includes both the Pamir Frontal Thrust, a fault formed by northward propagation of the Pamir with a Quaternary shortening rate of ~6–7 mm/a [*Li et al*., 2012, 2013a], and the Kashi-Atushi fold-and-thrust system, which formed by southward propagation of the southern Tian Shan with a Quaternary shortening rate of ~5 mm/a [*Chen et al*., 2002; *Scharer et al*., 2004; *Heermance et al*., 2008]. Active thrust faulting and folding is widely distributed across this zone (Figure 2). A geodetically defined convergence rate of ~7–9 mm/a [*Yang et al*., 2008; *Zubovich et al*., 2010; *Ischuk et al*., 2013] and the 1985 Wuqia *M*7.4 earthquake triggered by the Pamir Frontal Thrust reflect its ongoing and concentrated activity.

3. Active Flexural-Slip Faulting in the Mingyaole Anticline

3.1. The Mingyaole Anticline

The Mingyaole anticline is located at the western end of the Kashi-Atushi fold-and-thrust system and lies north of the Tuomuluoan and Mushi anticlines, segments of the Pamir Frontal Thrust (Figure 2). On the surface, the Mingyaole fold exhibits an E-W trending topographic relief that is ~35 km long by ~6–10 km wide (Figure 2). In the fold's western part, the Pleistocene conglomerate on the southern limb is overthrust by Paleogene gypsum of the Tuomuluoan anticline along the Pamir Frontal Thrust [*Li et al*., 2012]. To the east, the southern limb of the anticline was ruptured during the 1985 *M*7.4 Wuqia earthquake when slip occurred along the Mingyaole South Thrust, a northern branch of the Pamir Frontal Thrust (Figure 2) [*Feng*, 1994].

Lithified sedimentary sequences exposed in the Mingyaole fold include tan, brownish sandstone and mudstone of the Miocene (N1, Wuqia Group), gray-yellow and gray-green sandstone alternating with mudstone of the Pliocene (N2, Atushi Formation), and dark gray, massive pebble-cobble conglomerate of the Pleistocene (Q1, Xiyu Formation) (Figure 2). The Mingyaole fold is a simple, box-like fold with a steeper northern limb (~70°) and gentler southern limb (~58°) (Figure 3) [*Chen et al*., 2005; *Scharer et al*., 2006]. Total shortening and uplift along the Kalangoulvke water gap are ~1.7 km and ~2.3 km, respectively [*Li et al*., 2014]. Based on the initiation age of ~1.6 Ma from magnetostratigraphic dating [*Chen et al*., 2005]

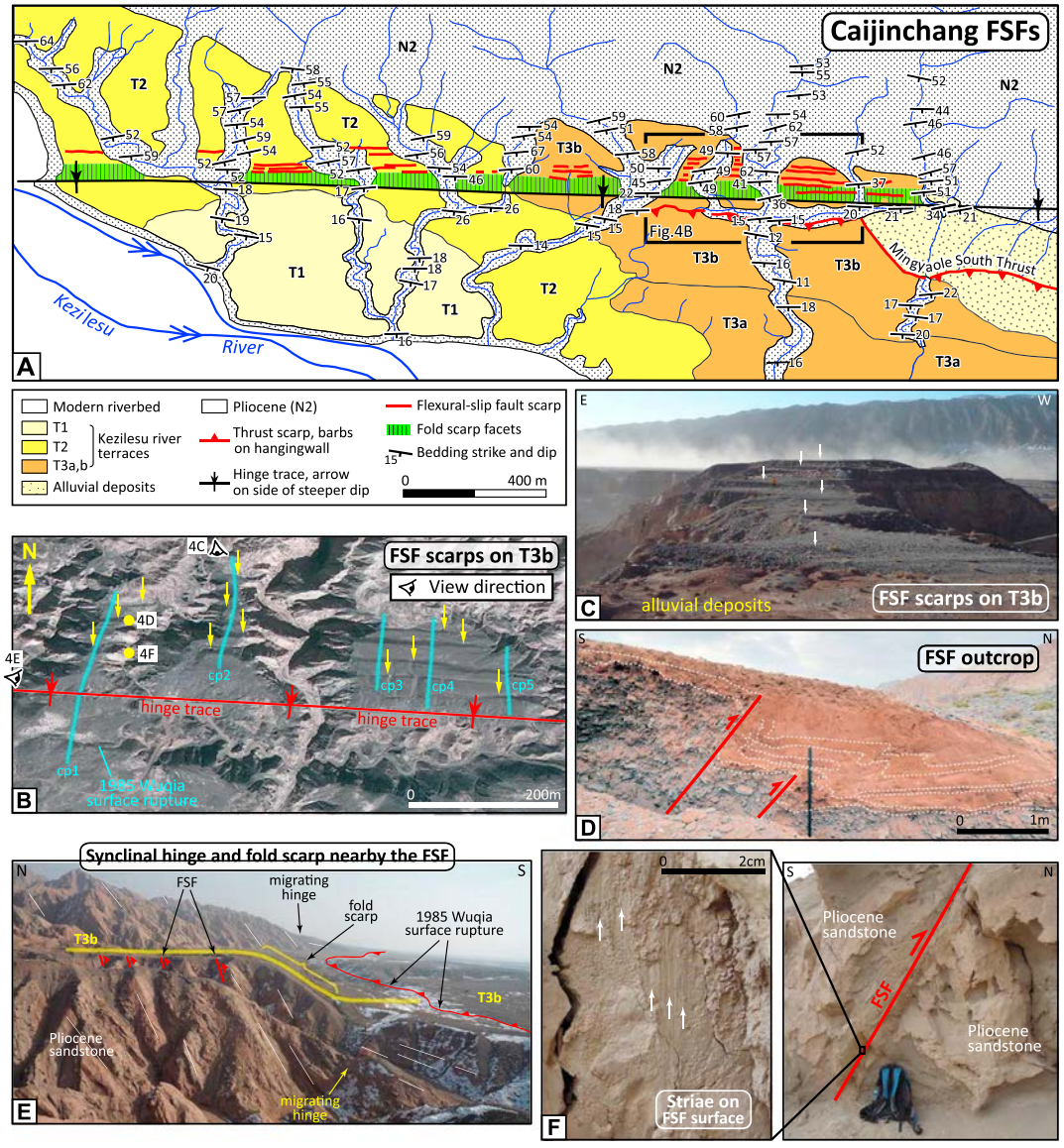

Figure 4. (a) Geologic and geomorphic map of the Kezilesu River terraces at Caijinchang on the southern limb of the Mingyaole fold, as interpreted from Google Earth images and field mapping. Mapping area shown in Figure 2. (b) Google Earth image of flexural-slip fault scarps (yellow arrows) and survey profiles. See Figure 4a for location. (c–f) Photographs of FSF scarps and outcrops. See viewpoints in Figure 4b.

and $^{26}Al/^{10}Be$ cosmogenic burial ages [*Thompson*, 2013], the average shortening rate and uplift rate have been estimated as ~1.1 mm/a and ~1.4 mm/a, respectively. The fold has remained active, and terrace surfaces crossing the fold not only are tilted [*Chen et al.*, 2005; *Scharer et al.*, 2006; *Li et al.*, 2013b] but also are deformed by a series of fold scarps and FSF scarps at Caijinchang and the Kalangoulvke water gap [*Yang et al.*, 2014; T. Li et al., under review, 2015].

3.2. Active FSFs at Caijinchang

Caijinchang is located on the southern limb of the Mingyaole fold and northern bank of the Kezilesu River (Figure 2), where, in response to uplift of the fold and reverse movement along the Mingyaole South Thrust, flights of strath terraces are incised into the Q1 conglomerate and the N2 sandstone (Figure 4a). These terraces are presently capped by gray well-rounded gravels, comprising clasts of limestone and sandstone with rare silt lenses. Based on the interpretation of Google Earth images and field observations, we categorized fluvial terraces into three major divisions with respect to their relative heights above the

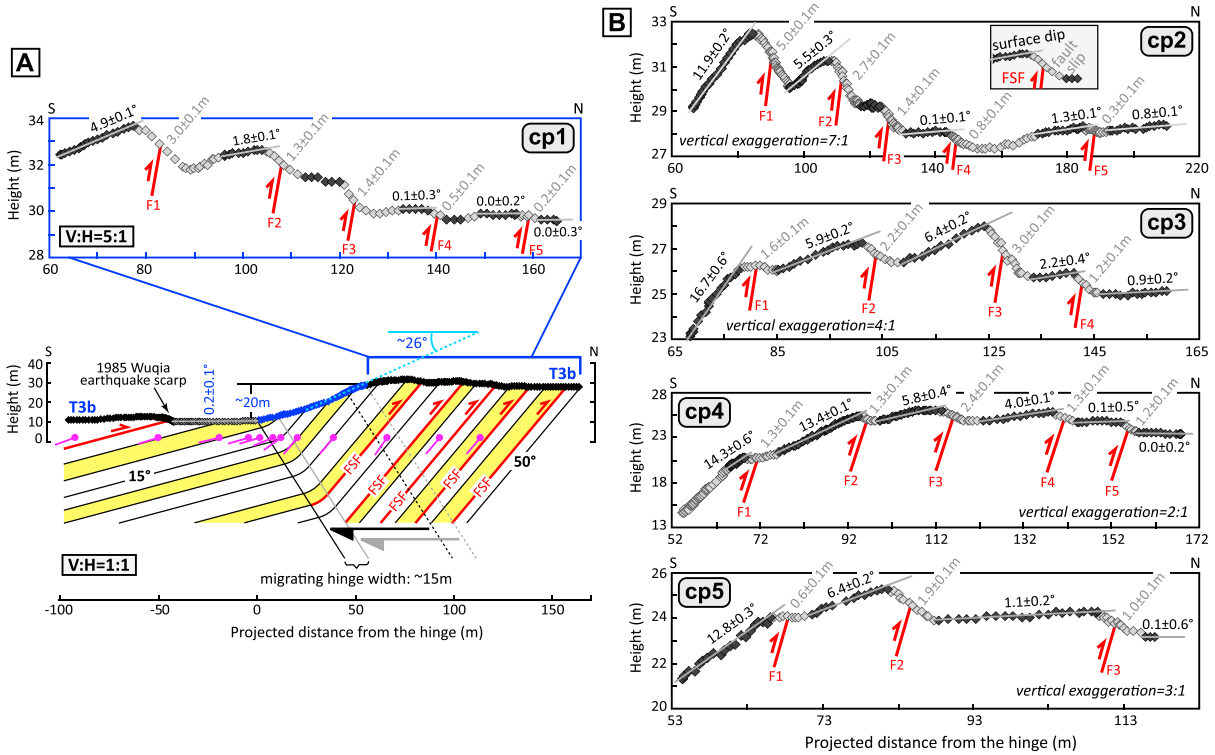

Figure 5. (a) Topographic survey of the fold scarp and FSF scarps; see Figure 4b for the location. Bed and FSF surface dips and terrace surface slopes with no vertical exaggeration (bottom). Profile with fivefold vertical exaggeration (top). (b) Topographic surveys of FSF scarps. FSF surface dips and terrace surface slopes are vertically exaggerated. Note that terrace surface slopes tend to decrease away from the hinge.

modern riverbed (Figure 4a). The T1 and T2 surfaces are ~8–15 m and ~30–40 m high, respectively. The T3 surface, ~15–20 m higher than the T2 surface, can be subdivided into the T3a and T3b, as distinguished by a height increase of ~3–5 m. At the front of the bedrock relief, the T3b surface is covered by brown, wedge-shaped alluvial deposits with a thickness of >1 m that pinch out quickly to the south (Figure 4c). According to ^{10}Be cosmogenic dating of *Thompson* [2013], the T2 surface has an exposure (abandonment) age of ~8.0 ka. Terrace surfaces are deeply cut by ephemeral channels, which flow southward into the Kezilesu River. We interpret the Caijinchang terraces to have been formed by Kezilesu River, rather than by these channels, because the capping terrace gravels are similar to those in the modern Kezilesu riverbed and because terrace risers are irregularly preserved along the Kezilesu River and are orthogonally crossed by these channels.

The south flowing ephemeral channels expose underlying bedrock. Geologic mapping of the bedrock defines an ~15 m wide synclinal hinge that separates beds dipping 50–59°S in the north from those dipping 15–20°S in the south (Figure 4a). On the T2 and T3b surfaces, and east trending, south facing topographic scarp coincides with and can be traced along the hinge (Figures 4a and 4e). The scarp height increases from ~16 m on the T2 surface to ~20 m on the T3b surface (T. Li et al., under review, 2015). The scarp slope on both surfaces dips ~26° (Figure 5a) and is comparable with the dip change of ~35° of the beds across the hinge. These characteristics indicate that the topographic scarp is a fold scarp kinematically formed by hinge migration, in which the beds and overlying terraces migrate from gentle (~15°S) to steep (~50°S) dip domains [*Suppe et al.*, 1992, 1997; *Chen et al.*, 2007b; *Hubert-Ferrari et al.*, 2007; T. Li et al., under review, 2015].

On the upper surface (north side) of the fold scarp where underlying beds dip steeply (~50–59°S), terrace surfaces are displaced by an array of ~0.2–5.0 m high, E-W trending, bed-parallel, north facing FSF scarps that display a clear stair-step geomorphology (Figures 4 and 5). The spacing between scarps ranges from 10 to 45 m, distributed across a <100 m wide zone on the T2 surface and <200 m wide zone on the T3b surface, to the north of the hinge (Figures 4b and 4c). The number and height of FSF scarps on T2 are less than those on T3b, although some scarps on T3b may be partially or totally covered by young alluvial deposits at the front of bedrock relief (Figure 4c). Fault planes exposed in terrace deposits dip ~50° to the

Table 1. Horizontal Distance to the Hinge, Terrace Surface Slope on the Hanging Wall, and Scarp Height of the Flexural-Slip Faults in the Mingyaole Fold

Profile No.	Fault No.	Distance (m)	Slope (deg)	Height (m)
cp1	F1	82	4.9 ± 0.1	3.0 ± 0.1
cp1	F2	107	1.8 ± 0.1	1.3 ± 0.1
cp1	F3	123	-	1.4 ± 0.1
cp1	F4	140	0.1 ± 0.3	0.5 ± 0.1
cp1	F5	158	0.0 ± 0.2	0.2 ± 0.1
cp1			0.0 ± 0.3	
cp2	F1	90	11.9 ± 0.2	5.0 ± 0.1
cp2	F2	112	5.5 ± 0.3	2.7 ± 0.1
cp2	F3	126	-	1.4 ± 0.1
cp2	F4	146	0.1 ± 0.1	0.8 ± 0.1
cp2	F5	186	1.3 ± 0.1	0.3 ± 0.1
cp2			0.8 ± 0.1	
cp3	F1	82	16.7 ± 0.6	1.6 ± 0.1
cp3	F2	103	5.9 ± 0.2	2.2 ± 0.1
cp3	F3	128	6.4 ± 0.2	3.0 ± 0.1
cp3	F4	143	2.2 ± 0.4	1.2 ± 0.1
cp3			0.9 ± 0.2	
cp4	F1	65	14.3 ± 0.6	1.3 ± 0.1
cp4	F2	92	13.4 ± 0.1	1.3 ± 0.1
cp4	F3	113	5.8 ± 0.4	2.4 ± 0.1
cp4	F4	139	4.0 ± 0.1	1.3 ± 0.1
cp4	F5	153	0.1 ± 0.5	1.2 ± 0.1
cp4			0.0 ± 0.2	
cp5	F1	68	12.8 ± 0.3	0.6 ± 0.1
cp5	F2	84	6.4 ± 0.2	1.9 ± 0.1
cp5	F3	112	1.1 ± 0.2	1.0 ± 0.1
cp5			0.1 ± 0.6	
kp1	F1	40.00	1.4 ± 0.1	1.1 ± 0.1
kp1			1.0 ± 0.2	
kp2	F1	245	2.9 ± 0.1	2.5 ± 0.1
kp2	F2	330	2.1 ± 0.1	0.9 ± 0.1
kp2	F3	383	1.4 ± 0.1	0.1 ± 0.1
kp2	F4	473	1.4 ± 0.1	0.9 ± 0.1
kp2	F5	524	1.36 ± 0.02	0.3 ± 0.1
kp2	F6	649	-	0.3 ± 0.1
kp2	F7	717	1.1 ± 0.1	0.6 ± 0.1
kp2	F8	887	1.1 ± 0.2	0.4 ± 0.1
kp2			0.64 ± 0.02	

south, similar to the underlying dip of the beds (Figure 4d). On bedrock outcrops, the fault surface displays bed-parallel slip and preserves striae with a rake of ~90° (Figure 4f).

Terrace surfaces not only are reversely displaced but also appear significantly tilted. To quantify the tilt angle, we surveyed terrace surfaces using an E-survey 660 Real-Time Kinematics differential GPS system which yields relative vertical and horizontal precisions of <4 cm (Figure 5), less than the geomorphic noise due to natural ground surface irregularities. Survey lines were roughly linear and avoided areas where the original terrace surface had been subsequently modified. Survey points were projected to a direction approximately perpendicular to the hinge, and the slopes were calculated using least squares linear regressions.

Along the surveyed profile cp1, the T3b segment south of the fold scarp and north of the Mingyaole South Thrust slopes 0.2 ± 0.1° to the south (Figures 4b and 5a). Because this segment is not obviously deformed, we use its slope to represent the original slope of the now-deformed T3b surface. Compared with this slope, the T3b surface tilts ~11–17° in the south and progressively decreases to ~4–7°, ~1–2°, and ~0–1° to the north (Figure 5a and Table 1). In each fault slice, the tilt direction of terrace surfaces is the same as the underlying dip of the beds, and the location of tilt angle variations coincides with the FSF scarps. Despite the tilting along each individual FSF, the entire faulted terrace surface may slope in either direction, depending on the relative slip along each FSF (Figures 4c and 5). During the 1985 Wuqia earthquake, one or two FSF scarps near the hinge were reactivated with a coseismic vertical displacement of ~0.2–0.3 m [*Feng*, 1994].

3.3. Active FSFs at Kalangoulvke Water Gap

The synclinal hinge at Caijinchang can be traced eastward to Kalangoulvke water gap (Figure 2), where terrace surfaces are also deformed by fold scarps and FSF scarps (Figure 6). At this site, three strath terraces of different ages are present (Figure 6a). The T1 and T2 surfaces are locally preserved, compared with the spatially extensive T3 surface. Subsequent erosion by ephemeral streams has produced deeply incised gullies into all of the terrace surfaces.

The synclinal hinge is ENE trending and ~16 m wide, separating beds dipping ~58°S in the north from those dipping ~16°S in the south (Figures 6a, 6d, and 6f). Height/slope of the fold scarp is ~6 m/~16° on the T1 surface and ~44 m/~26° on the T3 surface (Figures 6d and 6f) (T. Li et al., under review, 2015). On the T3 surface, at least nine FSF scarps are preserved in an ~900 m wide zone north of the

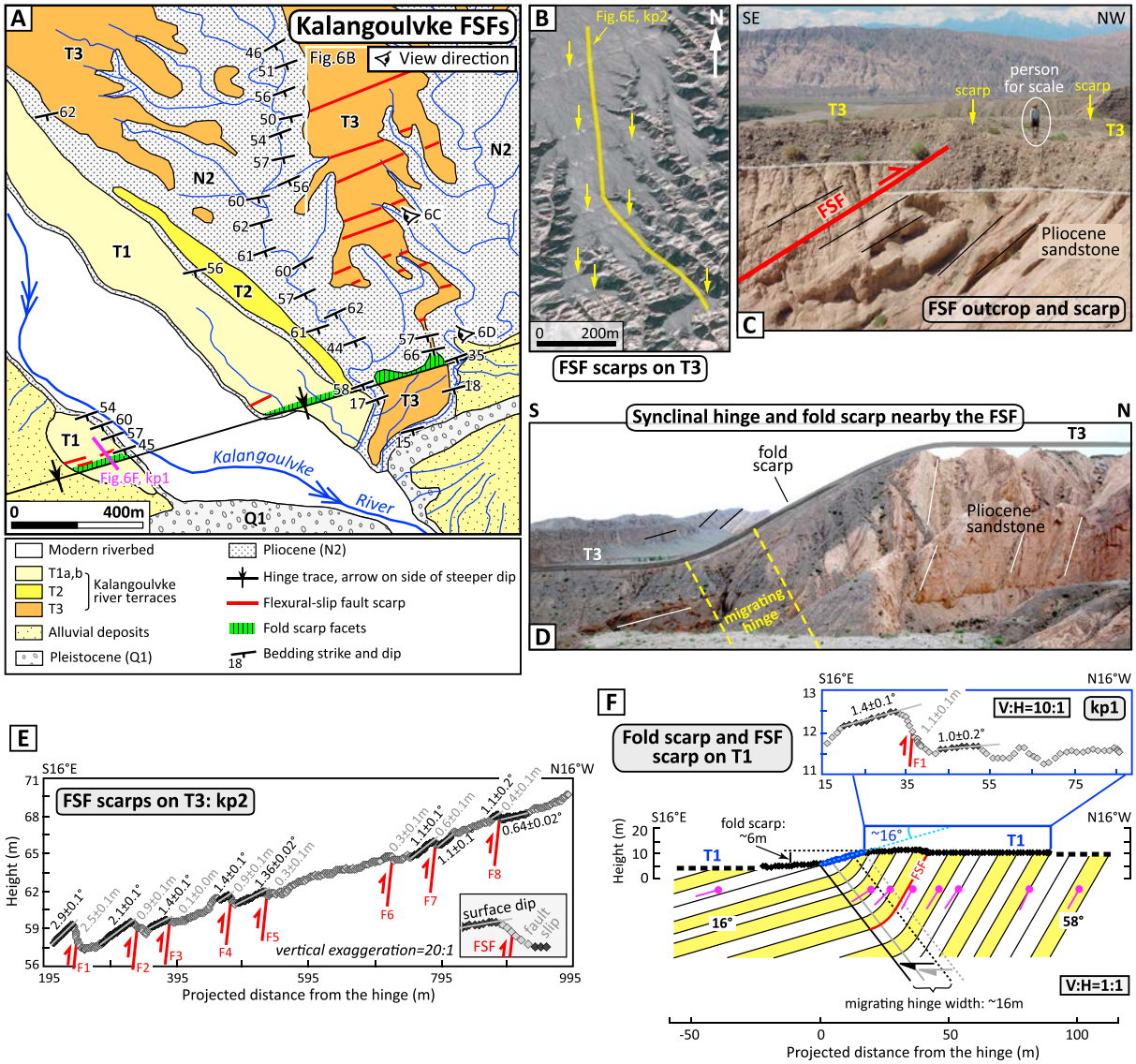

Figure 6. (a) Geologic and geomorphic map of the Kalangoulvke River terraces on the southern limb of the Mingyaole fold. See Figure 2 for location. (b) Google Earth image of FSF scarps (yellow arrows) and survey profile (kp2) on the T3 surface. (c) Photograph of the FSF (viewpoint in Figure 6a): fault scarp (yellow arrows) on the land surface, displaced strath, and underlying bedrock. (d) Synclinal hinge and fold scarp nearby FSF scarps on the T3 surface. See viewpoint in Figure 6a. (e and f) Topographic survey profiles of FSF scarps on the T3 and T1 surfaces, with locations shown in Figures 6b and 6a, respectively.

hinge, with spacing ranging ~50–160 m (Figure 6a and Table 1). Although some scarps are too small to be easily identified in the field, tan ponded deposits at the front of those scarps make them apparent as significant linear features in Google Earth images (Figure 6b). FSF scarps have been completely eroded near the fold scarp, but the locations of some of their fault planes can be roughly determined from the remaining terrace deposits and underlying bedrock. On the T1 surface, only two FSF scarps occur in a zone <50 m wide to the north of the hinge (Figure 6a). There, heights of FSF scarps vary from ~0.1 to 2.5 m, much smaller than those at Caijinchang (Figure 6f and Table 1). Compared with the modern riverbed slope of ~1.0° [*Chen et al.*, 2005; *Scharer et al.*, 2006], terrace surfaces are locally tilted to the south: tilt angles of the T3 surface are ~1–2° in the south and gradually decrease to ~0.4° and ~0–0.1° to the north. Although locally disturbed by nearby FSF scarps, the entire slope of the T3 surface is similar to that (~1.0°) of the riverbed, implying that the T3 surface and underlying beds are not obviously rotated.

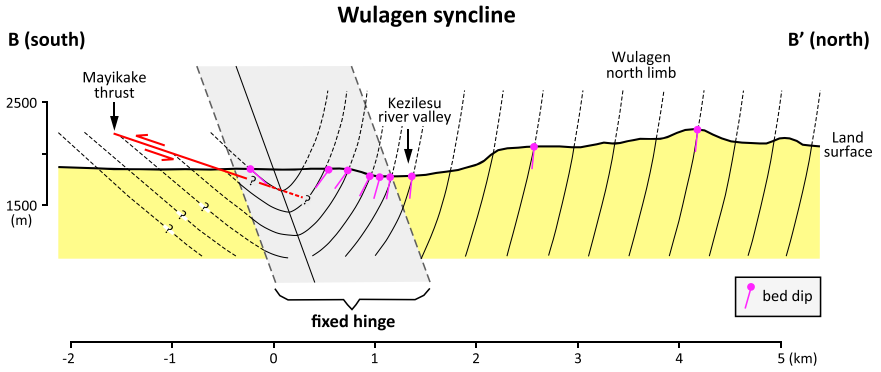

Figure 7. Geologic cross section along the Wulagen syncline (for location, see Figure 2). The hinge width is roughly constrained based on the zone across which the dip of underlying beds gradually changes from ~84°SW in the north to ~40°NE in the south. The subsurface geometry of the Mayikake Thrust is speculative.

4. Active Flexural-Slip Faulting in the Wulagen Syncline

4.1. The Wulagen Syncline

Located to the west of the Mingyaole anticline and north of the Pamir Frontal Thrust, the Wulagen syncline is the northern boundary of an intramontane basin formed by the irregular collisional interface of the Pamir and the Tian Shan (Figure 2). In the fold's northern limb, the north flowing Biertuokuoyi River and south flowing Kangsu River join with the east flowing Kezilesu River, which deposited ~10 to 40 m thick fluvial gravels and formed a basin-wide Last Glacial Maximum terrace (LGM terrace, Figure 2) [*Li et al.*, 2012]. New ^{10}Be cosmogenic dating of the LGM terrace gives an exposure (abandonment) age of ~15.4 ka [*Thompson*, 2013].

The Wulagen syncline trends ESE (Figure 2). The fold's northern limb is a well-exposed, simple, subvertical monocline composed of ~7–8 km of Neogene sandstone and Pleistocene conglomerate (Figures 2 and 7). Comparatively, the fold's core and southern limb are poorly exposed, because much of this zone is obscured by thick fluvial deposits. Geologic mapping of scattered outcrops roughly defines a ~1500 m wide hinge, across which the bed gradually changes from ~80 to 86°SW dips in the north to dips of ~40°NE in the south (Figures 7 and 8a). Still farther north, the fold connects with an anticline.

The fold's southern limb is displaced by the south vergent Mayikake Thrust (Figures 2, 7, and 8a) [*Li et al.*, 2012] to create a series of east trending, south facing (opposite to the slope of the LGM terrace), ~7.5 to 15 m high fault scarps on the LGM terrace. Since exposure of the LGM terrace, the dip-slip rate of the thrust is ~3.6 mm/a [*Li et al.*, 2012; *Thompson*, 2013]. The Mayikake Thrust may be an emergent master fault controlling the Wulagen fold, a bending moment thrust secondarily generated by the Wulagen fold and vanishing with depth, or it could be a fault that is kinematically independent from the Wulagen fold. Due to a lack of subsurface data, it is difficult to unambiguously determine the geometric relationship of these two structures.

4.2. Active Flexural-Slip Faulting

Fluvial terraces across the Wulagen fold can be divided into three distinct age groups (Figure 8a). The height of the T1 and T2 surfaces are ~3–5 m and ~30–40 m above the modern riverbed, respectively. The T3 surface can be correlated with the LGM terrace and can be subdivided into the T3a, with a surface height of $>$60 m, and the T3b, whose surface is ~4–5 m higher than that of the T3a. Bedrock underlying fluvial deposits is dominated by Pleistocene massive conglomerate.

Two groups of subparallel, SE trending FSF scarps transect the terrace surface (Figure 8a). The northern group of north facing FSF scarps displaces the T3 and T1 surfaces and even the riverbed (Figures 8a, 8b, 8d, and 8e), implying strong activity in the recent times. In comparison, the southern group of south facing FSF scarps is much smaller (Figures 8a and 8c). These two groups of scarps trend 40°NW in the west and rotate gradually eastward to 70°NW. Some FSF scarps are difficult to distinguish from paleochannels because they have similar trends (Figures 8b and 8e). In the context of the underlying structure, the north facing and south

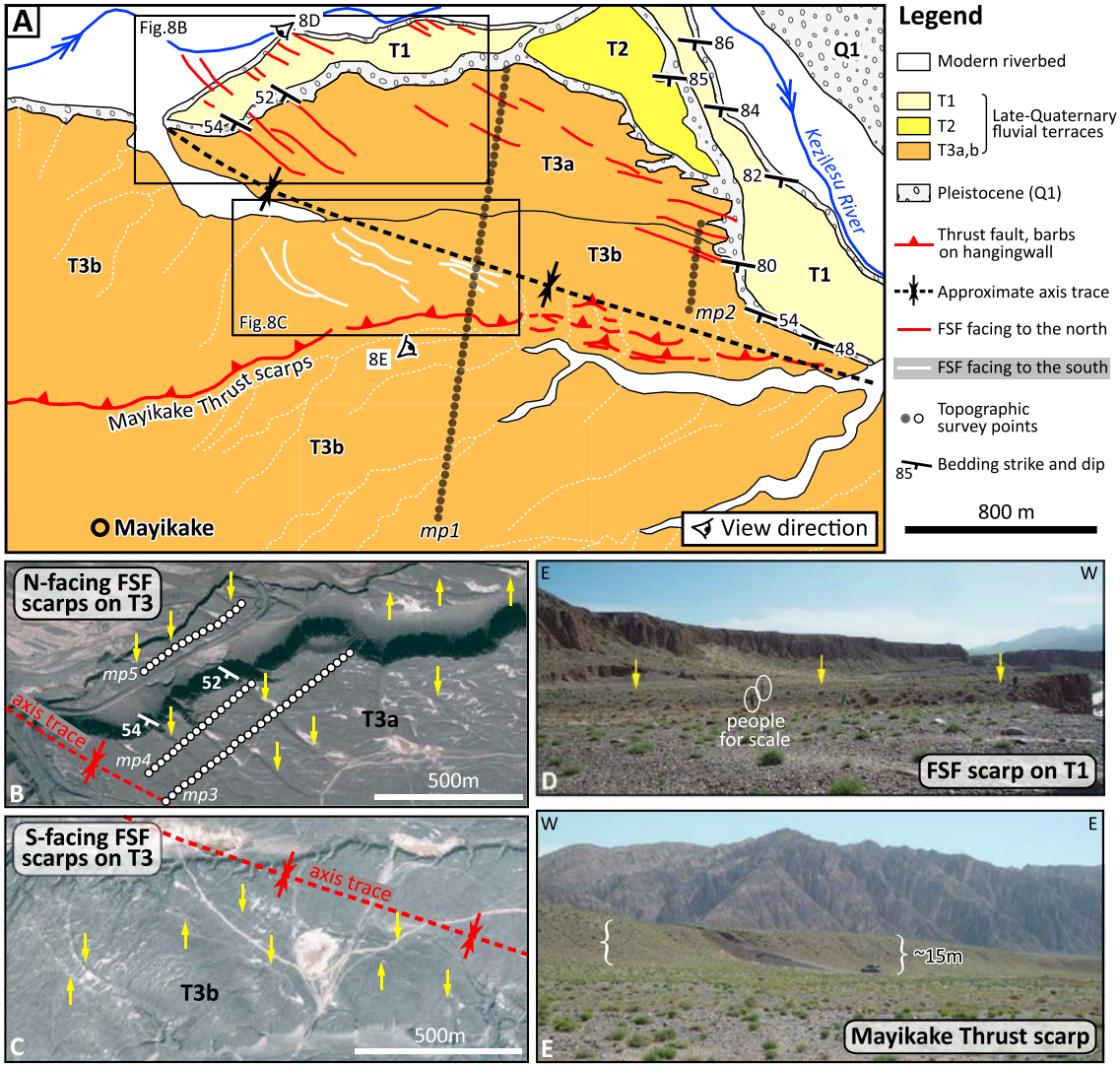

Figure 8. (a) Geologic and geomorphic map of the Kezilesu River terraces in the Wulagen fold. Location shown in Figure 2. (b and c) Google Earth images of FSF scarps (yellow arrows) on the T3 surface. Locations shown in Figure 8a. (d) Photograph (viewpoint in Figure 8a) of the FSF scarp (yellow arrows) on the T1 surface. (e) Photograph (viewpoint in Figure 8a) of the ~15 m high Mayikake Thrust scarp on the T3 surface (LGM terrace surface).

facing scarps are located north and south of Wulagen's synclinal hinge, respectively, and coincide with the trend of the hinge (Figures 7 and 8a). Compared to the Mingyaole FSFs, the Wulagen FSFs on the T1 surface are much lower than those on the T3 surface, yet their number and distribution width are similar.

FSF scarps to the north of the hinge are ~0.3–4.2 m high on the T3 surface and ~1.2–2.4 m high on the T1 surface (Figure 9 and Table 2). To the south of the hinge, the FSF scarps are merely ~0.3–0.6 m high on the T3 surface. The spacing of FSF scarps on both sides ranges from several tens of meters to a few hundreds of meters (Table 2). As seen at Caijinchang, the faulted terrace surfaces are obviously tilted (Figure 9). Along the profile mp1, the T3b surface in the footwall of the Mayikake Thrust slopes northward $-0.5 \pm 0.1°$, a slope we assume to represent the original slope of all terrace surfaces, because the T3b surface of this segment is not obviously disturbed by active structures. Compared with this slope, the terrace surface to the north of the hinge is back tilted (to the south: opposite to the original terrace slope), and the terrace surface to the south of the hinge is tilted (to the north: in the same direction as the original terrace slope). Northward farther away from the hinge, the tilt angle of the T3 surface gradually decreases from ~4–5° near the hinge to ~3–4°, ~2–3°, ~1–2°, and ~0–1°, and the T1 surface tilts from ~1.9° to ~1.0° and ~0.8°.

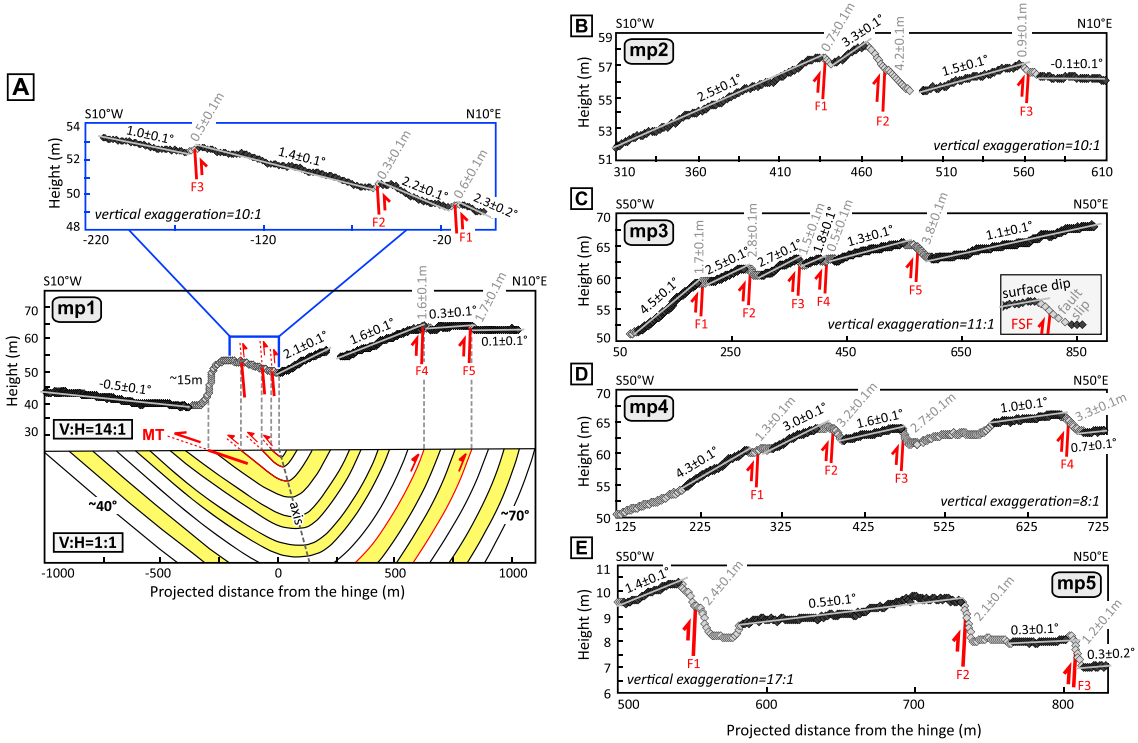

Figure 9. Topographic profiles of the FSF scarps on the Kezilesu River terraces in the Wulagen fold. See Figures 8a and 8b for locations. MT: Mayikake Thrust.

Table 2. Horizontal Distance to the Hinge, Terrace Surface Slope on the Hanging Wall, and Scarp Height of the Flexural-Slip Faults in the Wulagen Fold

Profile No.	FSF No.	Distance (m)	Slope (deg)	Height (m)
mp1	F1	−160	−1.4 ± 0.1	0.5 ± 0.1
mp1	F2	−60	−2.2 ± 0.1	0.3 ± 0.1
mp1	F3	−13	−2.3 ± 0.1	0.6 ± 0.1
mp1	F4	630	1.6 ± 0.1	1.6 ± 0.1
mp1	F5	830	0.3 ± 0.1	1.7 ± 0.1
mp1			0.1 ± 0.1	
mp2	F1	435	2.5 ± 0.1	0.7 ± 0.1
mp2	F2	475	3.3 ± 0.1	4.2 ± 0.1
mp2	F3	562	1.5 ± 0.1	0.9 ± 0.1
mp2			−0.1 ± 0.1	
mp3	F1	250	4.5 ± 0.1	1.7 ± 0.1
mp3	F2	330	2.5 ± 0.1	2.8 ± 0.1
mp3	F3	413	2.7 ± 0.1	1.5 ± 0.1
mp3	F4	455	1.8 ± 0.1	0.5 ± 0.1
mp3	F5	525	1.3 ± 0.1	3.8 ± 0.1
mp3			1.1 ± 0.1	
mp4	F1	290	4.3 ± 0.1	1.3 ± 0.1
mp4	F2	390	3.0 ± 0.1	3.2 ± 0.1
mp4	F3	473	1.6 ± 0.1	2.7 ± 0.1
mp4	F4	675	1.0 ± 0.1	3.3 ± 0.1
mp4			0.7 ± 0.1	
mp5	F1	550	1.4 ± 0.1	2.4 ± 0.1
mp5	F2	735	0.5 ± 0.1	2.1 ± 0.1
mp5	F3	809	0.3 ± 0.1	1.2 ± 0.1
mp5			0.3 ± 0.2	

Southward farther away from the hinge, the tilt angle of the T3b surface gradually decreases from ~−1.8° to ~−1.7°, ~−0.8°, and ~−0.5° (Figure 9 and Table 2).

5. Discussion

5.1. Deformation and Distribution Characteristics

FSF scarps in the Mingyaole and Wulagen folds reveal key information on the deformational and spatial characteristics of active flexural-slip faulting. Both Mingyaole and Wulagen FSF scarps lie near the synclinal hinge (Figures 4–9), consistent with observations at other sites [*Yeats et al.*, 1981, 1997; *Rockwell et al.*, 1984; *Ishiyama et al.*, 2004; *Kelsey et al.*, 2008]. In field surveys of these two folds, we found no reliable FSF scarps near the anticlinal hinges. The absence of FSF scarps near these hinges in our study area appears contradictory to the results of analogue models and observations

of well-lithified outcrops [e.g., *Tanner*, 1989; *Sanz et al*., 2008], where flexural-slip faulting was shown to occur near the anticlinal hinge. The reason for this discrepancy remains unclear. One possibility is that flexural-slip faulting near the anticlinal hinge may be too weak to produce significant topographic expressions, compared with that near the synclinal hinge.

Across an active hinge, the beds on both sides of the Mingyaole hinge dip unidirectionally (Figures 4–6). The beds on the south of the hinge continue to dip south, albeit at a gentler angle than the beds on the north side. In contrast, the beds on two sides of the Wulagen hinge dip in opposite directions and dip approximately symmetrically toward the hinge (Figures 8 and 9). The Mingyaole hinge has migrated, producing a series of fold scarps on the land surface, whereas the Wulagen hinge is fixed, and no similar topographic scarp is present. The Mingyaole hinge is relatively narrow (~15 m) and angular; thus, its width is negligible when comparing the distance from the FSF scarp to the hinge. Comparatively, the Wulagen hinge is wide (~1500 m) and curved, and its width should be considered. Based on these observations, we would expect that active FSF scarps can occur irrespective of whether the beds on either side of the hinge dip in one direction or in opposite directions, whether the hinge is migrating or fixed, or whether the hinge shape is narrow and angular or wide and curved.

With respect to the dip of underlying beds, active FSFs are more likely to produce higher scarps on steeper beds. In the Mingyaole fold (Figures 4–6), FSF scarps are clearly present on the ~50–58°S domain of underlying beds, whereas no scarps are observed on the gentler domain of ~15–16°S. In the Wulagen fold (Figure 7–9), FSF scarps are present on both dip domains; however, scarps on the steeper (~70°SW) domain are much larger than those on the gentler (~40°NE) domain. These observations suggest that active FSFs favor steep beds and that for any given increment of folding during seismic or aseismic events, the steeper beds may be energetically more advantageous to focus slip [*Ramsay*, 1967; *Johnson and Johnson*, 2000; *Sanz et al*., 2008].

From a spatial perspective, the Mingyaole FSF scarps on the higher terrace surfaces are more widely distributed (spanning $<$200 m on Caijinchang's T3b surface and ~900 m on Kalangoulvke's T3 surface) than those on lower terrace surfaces (spanning $<$100 m on Caijinchang's T2 surface and $<$50 m on Kalangoulvke's T1 surface). In the Wulagen fold, however, the number, spacing, and distribution width on higher and lower terrace surfaces are similar, even though the scarp heights differ. We speculate that slips on the Mingyaole FSFs may not have been simultaneous on all such faults and those closer to the hinge may slip more readily, whereas the Wulagen FSF scarps may have formed synchronously and randomly in space.

In the Mingyaole and Wulagen folds, terrace surfaces near to active FSFs are tilted in the same direction as the dip of underlying beds. For example, the Wulagen terrace surface is back tilted (to the south) on the north side of the hinge and is tilted on the south side of the hinge, displaying a broad, upward concave shape (Figure 9a). The tilt of terrace surfaces may arise from (i) limb rotation [*Poblet and McClay*, 1996; *Suppe et al*., 1997, 2004; *Scharer et al*., 2006]; (ii) listric thrusting [*Amos et al*., 2007]: if the dip of a fault plane decreases gradually with depth, overlying terrace surfaces will be tilted as well; and (iii) flexural-slip faulting [*Yeats et al*., 1981, 1997; *Rockwell et al*., 1984], whereby the tilt of terrace surface results from decreasing slip and dip along the fault plane toward the hinge. On Mingyaole's southern limb, although locally tilted near the FSF scarps, the overall slope of terrace surfaces displays no obvious tilt (Figure 6) and is even back tilted (Figure 5a), compared with its original slope. This pattern is inconsistent with limb rotation, and we conclude that the tilt of terrace surface is a result of flexural-slip faulting. In the Wulagen fold, terrace surfaces may be tilted by a combination of limb rotation of an underlying blind thrust, listric thrusting of the Mayikake Thrust, and flexural-slip faulting.

Another notable feature of terrace deformation is the changing tilt angle of the individually deformed terrace surfaces. The tilt angles gradually decrease with distance from the hinge, and the abrupt changes of tilt angle coincide with the FSF scarps. Because both limb rotation and listric thrusting can merely tilt terrace surfaces at unique or gradually changing angles [*Poblet and McClay*, 1996; *Suppe et al*., 1997, 2004; *Scharer et al*., 2006; *Amos et al*., 2007], we ascribe the abrupt change of tilt angle to the kinematics of flexural-slip faulting, whereby terrace surfaces closer to the hinge are influenced and tilted by more active FSFs. For example, along profile cp5 at the Mingyaole fold (Figure 5a), the terrace segment overlying fault F1 is likely to be tilted not only by the fault F1 but also by the slip along F2 and F3. Comparatively, the terrace segment

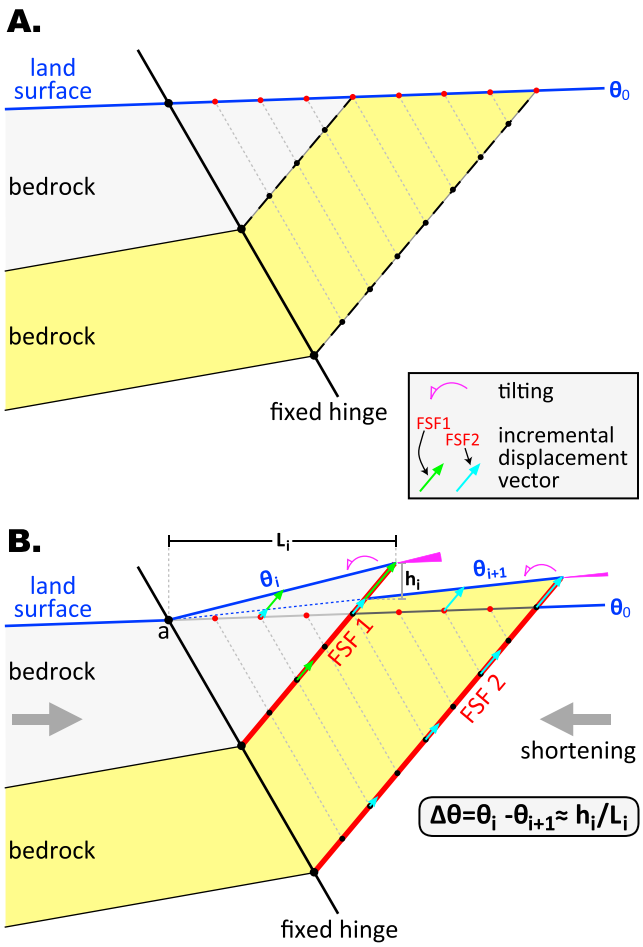

Figure 10. Kinematic model of active flexural-slip faulting with a fixed, angular hinge. (a) Land surface with original slope θ_0 overlying kink-folded bedrock with a fixed hinge. Beds on either side of the hinge dip in the same direction. The contact of beds with different strengths is the potential slip surface. (b) During shortening, FSFs are activated, and the original surface is displaced and tilted in the same direction as underlying bedrock dips. θ_i and θ_{i+1} are land surface slopes. Note that slip along the fault plane linearly decreases to zero at the hinge. Slip vector of any point on the fault plane is equal to that on the land surface above it. Land surface segment between the FSF1 and FSF2 is tilted only by the FSF2, whereas the segment between the FSF1 and the hinge is tilted by a combination of the FSF1 and FSF2. Both segments are tilted around the same circle center of the point "a." Surface tilt (due to FSF motion) and overall slope decrease away from the hinge. The land surface slopes (θ_i and θ_{i+1}), the FSF scarp height (h_i), and the horizontal distance (L_i) between the FSF and the hinge have a predictable geometric relationship (equation (1)).

between the F1 and F2 is only tilted by faults F2 and F3, and the terrace segment between the F2 and F3 is only tilted by the fault F3.

5.2. Kinematic and Geometric Models

The observed deformational and spatial characteristics indicate that the deformation of terrace surfaces crossing active FSFs is inherently correlated with the active hinge. We develop three kinematic and geometric models to explain how different hinge shapes influence surface expression of active FSFs: the *fixed angular hinge model*, the *migrating angular hinge model*, and the *fixed curved hinge model*. The first model is the simplest one and the basis of two others.

For the fixed angular hinge model (Figure 10), the hinge is fixed, and its width can be ignored in comparison to the distance from the FSF scarp to the hinge. The land surface overlying the more steeply dipping beds will be displaced as the FSF is activated through bed-parallel slip. As slip along the fault plane decreases to zero at the fold hinge [*Ramsay*, 1967; *Yeats et al.*, 1981, 1997; *Johnson and Johnson*, 2000; *Sanz et al.*, 2008], we assume that this decrease is simply linear. Then each segment of the land surface on the hanging wall is tilted at a constant angle, and different segments are tilted around the same rotation center (Figure 10b). Because the segment closer to the hinge is influenced by a greater number of underlying FSFs, the tilt angle of more distant segments decreases farther away from the hinge. Land surface slopes (θ_i and θ_{i+1}), scarp height (h_i), and horizontal distance away from the hinge (L_i) of the FSF (i) have a geometric relationship (see Appendix A):

$$\Delta\theta = \theta_i - \theta_{i+1} \approx \frac{h_i}{L_i} \tag{1}$$

For the migrating angular hinge model (Figure 11), the hinge width can be ignored, but the hinge can migrate. During active hinge migration, the land surface is deformed by the growing fold scarp (Figures 11b1 and 11c1), whose height and slope can be geometrically predicted (T. Li et al., under review, 2015). Similar to the first model (Figure 10b), the FSFs can be activated in beds that are more steeply dipping, and the land surface is tilted due to decreasing slip along the fault plane toward the hinge. As the

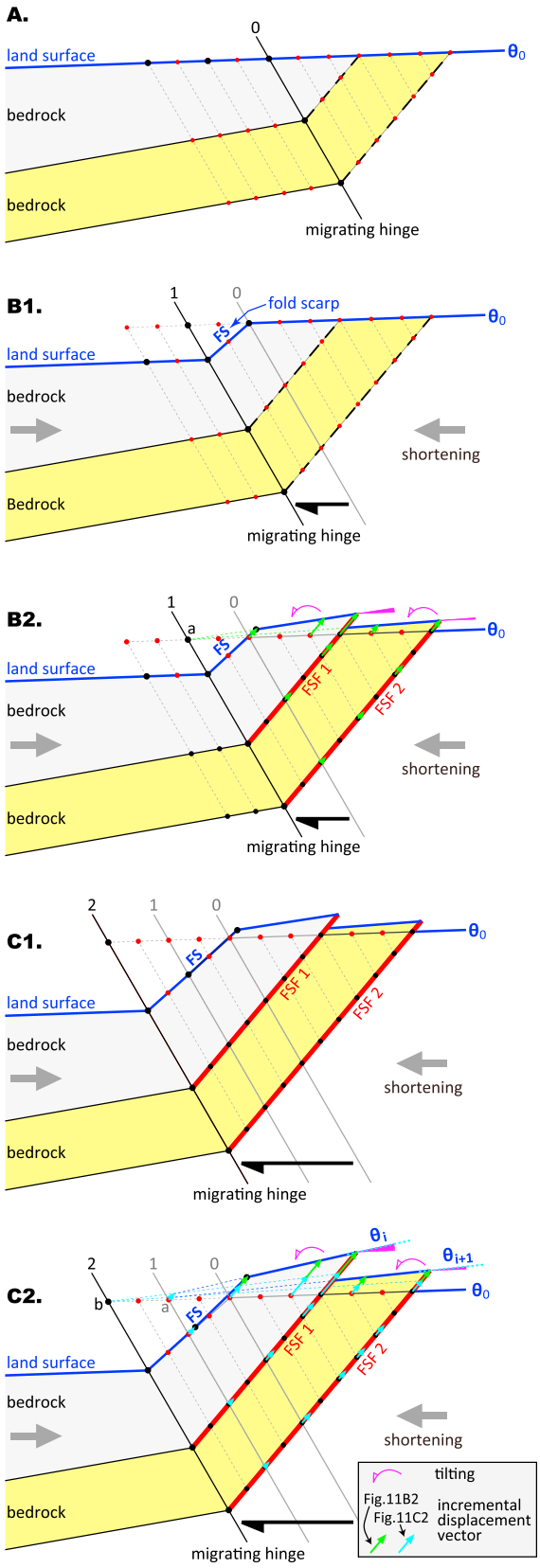

hinge gradually migrates, the FSF scarp height and tilt angle of the land surface increase. This model predicts the geometric relationship for changing surface dip (see Appendix A):

$$\Delta\theta = \theta_i - \theta_{i+1} \geq \frac{h_i}{L_i} \tag{2}$$

Note that the flexural-slip faulting can influence both the height and slope of the fold scarps (Figures 11b2 and 11c2).

For the fixed curved hinge model (Figure 12), the hinge is fixed, but its width is considerable. Along the curved hinge, therefore, the FSF acts as a listric thrust with a dip that becomes gentler at greater depths (Figure 12b). Overlying the curved fault plane segment, the land surface is tilted at increasingly higher angles farther away from the hinge due to a combination of fault slip and fault dip that decrease with depth. The surface slope follows this geometric relationship (Figure 12b):

$$\Delta\theta = \theta_i - \theta_{i+1} \geq \frac{h_i}{L_i} \tag{3}$$

Beyond the curved fault plane segment, the land surface is tilted around the same circle center and has a constant angle. The surface slope has the geometric relationship (Figure 12b):

$$\Delta\theta = \theta'_i - \theta'_{i+1} \approx \frac{h'_i}{L'_i} \tag{4}$$

Figure 11. Forward models of active flexural-slip faulting with a migrating angular hinge. (a) Initially, a planar land surface spans across a migrating angular hinge. On either side of the hinge, the beds dip in the same direction. (b) As the hinge migrates to position *1*, the land surface is deformed by a fold scarp (FS), displaced by activated FSFs, and tilted in the same direction as the dip of the underlying bedrock. In order to more easily analyze and illustrate this process, we divide it into two steps. (b1) The hinge migrates to position *1* and forms a fold scarp on the land surface. The height of fold scarp can be used to constrain incremental shortening of the fold, and the slope of fold scarp is dependent on underlying bedrock dips (T. Li et al., under review, 2015). (b2) The FSFs are reactivated, and the land surface is displaced and tilted. The land surface segments between hinge position 0 and FSF1 and between FSF1 and FSF2 are tilted around the same center point a. Note that the fold scarp height and slope are slightly influenced in this process. (c) The hinge migrates to position 2. (c1) The fold scarp grows progressively with increasing height and roughly constant slope. (c2) The land surface continues to be displaced and tilted. Land surface segments are tilted around the same center point "b," and the fold scarp height and slope are influenced again.

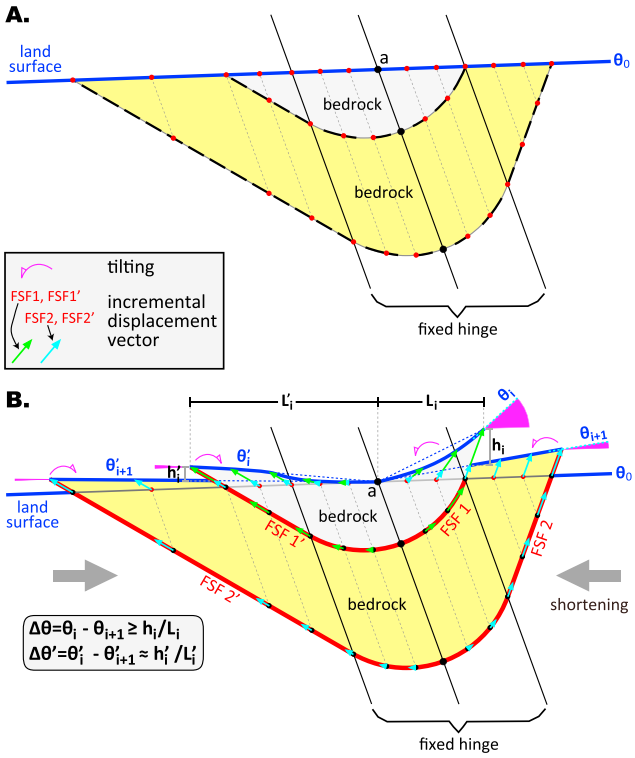

Figure 12. Kinematic model of active flexural-slip faulting with fixed curved hinge. (a) Initially, a land surface spans across a syncline with a fixed, curved hinge. The beds on either side of the hinge dip in opposite directions. The hinge width is considerable. (b) The FSF is activated, and its curved segment creates a listric thrust whose dip becomes gentler at depth. Along the curved fault plane segment, the slip amount decreases toward the hinge, and the slip direction rotates toward the hinge. The slip vector of any point on the fault plane is equal to that on the land surface directly above it. Overlying the curved fault plane segment, the land surface is tilted by increasing angles farther away from the hinge due to a combination of fault slip and fault dip that decrease toward both depth and the hinge. Beyond the curved fault plane segment, the land surface is tilted around the center point a. Note that the FSF scarp height and tilt angle of the land surface on the more steeply dipping (right) side are larger than those on the more gently dipping (left) side.

5.3. Mingyaole and Wulagen Flexural-Slip Faults

At the Mingyaole fold, the hinge width is only ~15 m (Figures 4–6), much smaller than the distance from the FSF scarps to the active hinge (≫40 m). The hinge has migrated and produced a series of fold scarps on terrace surfaces. Therefore, the Mingyaole FSFs can be approximated by the migrating angular hinge model. Consistent with the prediction of the geometric model (equation), the observed fault and geomorphic parameters indicate that almost all changes in slope angle ($\Delta\theta$) are larger than the height of the scarp divided by the horizontal distance to the hinge (h_i/L_i) (Figure 13).

At the Wulagen fold, the hinge is fixed and its width is ~1500 m. This distance is comparable to that from the FSF scarp to its hinge, thus making it suited to the fixed curved hinge model. Because almost all FSFs are in the active hinge zone and their fault planes are curved (Figures 7 and 9a), the FSF has the same geometric relationship as predicted by equation (3) (Figure 13).

Active FSFs can play a regionally significant role in accommodating folding deformation [*Yeats*, 1981, 1997; *Rockwell et al.*, 1984; *Niño et al.*, 1998; *Ishiyama et al.*, 2004, 2007; *Kelsey et al.*, 2008]. At Caijinchang of the Mingyaole fold (Figures 4 and 5 and Table 1), the total north vergent slip accommodated by FSFs since exposure of the T3b surface is ~9–13 m, based on the summed height of ~8–10 m of these scarps and the fault plane dips of ~50–60°. This amount can be compared to the incremental shortening of ~13 m absorbed by the T3b fold scarp (T. Li et al., under review, 2015). Based on the T2 exposure age of ~8.0 ka, the summed dip-slip rate of the FSFs is <~1.3 mm/a. In the Wulagen fold (Figure 9 and Table 2), the total NE vergent slip consumed by FSFs since exposure of the T3 and T1 surfaces is ~10 m and ~6 m, respectively, and the total SW vergent slip since exposure of the T3b surface is ~1.5 m. Considering that the T3 has an exposure age of ~15.4 ka, the summed NE and SW vergent dip-slip rates are ~0.7 mm/a and ~0.1 mm/a, respectively. Although the quantitative relationship between the amount of bed-parallel slip and the fold shape is not precisely defined, our field observations confirm these mechanical interpretations of flexural-slip faults as capable of effectively accommodating significant folding deformation.

5.4. Implications for Seismic Hazards Associated With Active Blind Thrusts

Unlike emergent faults, which can rupture the surface and produce geomorphic scarps during large earthquakes, active blind thrusts produce near-surface deformation across a widely distributed zone by folding. The lack of a well-defined surface expression commonly makes it difficult to accurately determine whether the blind thrust is active or not, to choose an appropriate width for the setback zone for

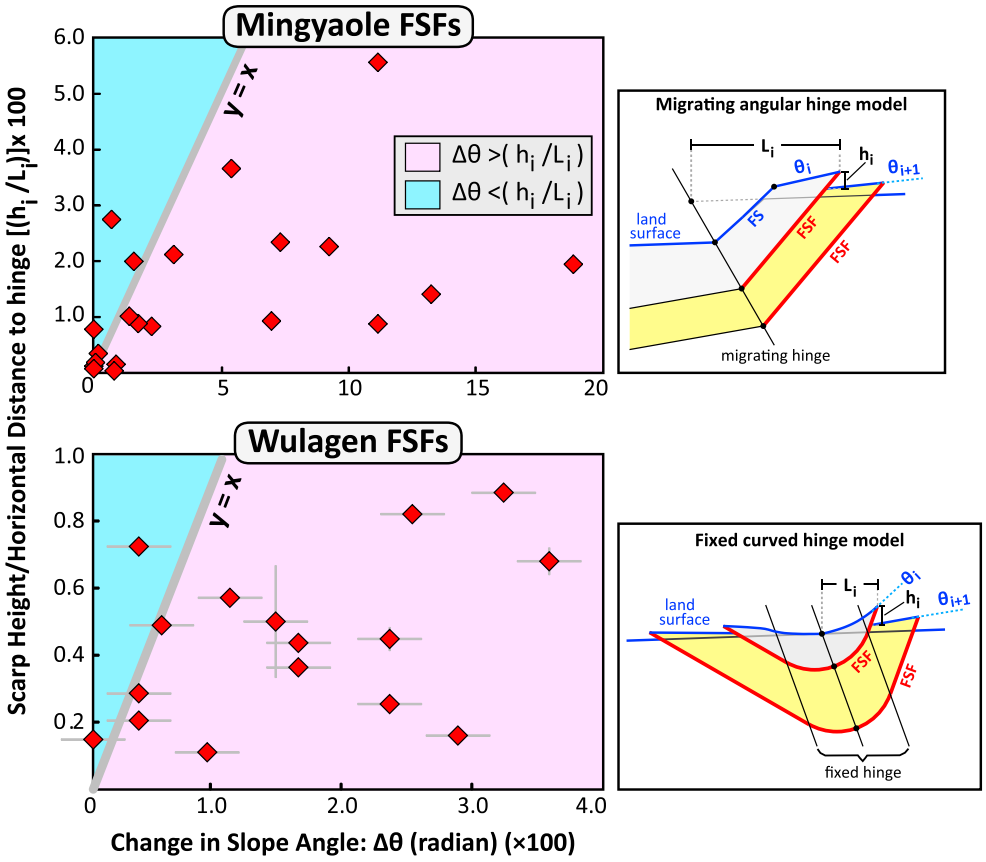

Figure 13. Relationship of the change in slope ($\Delta\theta = \theta_i - \theta_{i+1}$) versus scarp height ($h$) divided by horizontal distance to the hinge (L) (h_i/L_i) for FSFs in the Mingyaole and Wulagen folds. θ_i and θ_{i+1} are the land surface slopes on two sides of the flexural-slip fault. Note that >80% of the ratios of $\Delta\theta$ to (h_i/L_i) are >1. FS: fold scarp.

construction and safety purposes, and to preserve coseismic deposits that can be used to reconstruct the fault's paleo-earthquake history. Ubiquitously distributed and well-preserved FSF scarps can provide useful and relevant information to address these issues.

During the folding process, the land surface is inevitably deformed. Whether the fold and its blind thrust are active or not can be determined as a function of tilting and uplift of the land surface [e.g., *Rockwell et al.*, 1988; *Avouac et al.*, 1993; *Molnar et al.*, 1994; *Lavé and Avouac*, 2000; *Scharer et al.*, 2006; *Li et al.*, 2013a, 2013b], creation of fold scarps [e.g., *Thompson et al.*, 2002; *Ishiyama et al.*, 2004, 2007; *Chen et al.*, 2007b; *Hubert-Ferrari et al.*, 2007; *Li et al.*, 2014; T. Li et al., under review, 2015], and derangement of drainage parameters [e.g., *Kirby and Whipple*, 2012; *Amos and Burbank*, 2007; *Goode and Burbank*, 2011]. Comparatively, FSF scarps can be much easier to preserve, more readily apparent, and more reliable when used to determine the fold's activity.

Coseismic surface deformation across an active fold controlled by a blind thrust is strikingly different from that across a fault scarp produced by an emergent fault. A fault scarp can absorb almost all deformation in a narrow zone, and it is acceptable to delineate a narrow (perhaps few tens of meters) "setback zone" across the emergent fault. In contrast, deformation of an active fold is commonly distributed across a much wider zone. In the study of the 1999 Taiwan Chi-Chi earthquake, *Chen et al.* [2007b] suggested a setback zone exceeding ~100 m near the active fold scarp and its associated hinge. Besides singular fold scarps that accommodate large coseismic deformation and its associated hinge, active FSFs can produce seismic damage [*Yeats et al.*, 1981, 1997] due to at least two aspects: surface rupture along the fault and tilting on its hanging wall. Therefore, when selecting a distance for the setback zone, not only the active hinge but also the active FSFs on both sides should be considered. At the Mingyaole fold, the width of the active hinge and fold scarp is merely ~15 m and ~40 m (Figures 4–6), respectively; however, the FSF

scarps occur across a zone extending nearly 1000 m away from the hinge. At the Wulagen fold, the hinge width is ~1500 m (Figure 8), and the FSF scarps occur within a zone >1000 m. These observations indicate that a much wider setback zone, perhaps exceeding ~1000 m, is needed to mitigate hazards associated with active FSFs.

Active FSFs also provide a possible approach to constrain the paleo-earthquake history of active blind thrusts. The distributed deformation of the active fold overlying the blind thrust commonly makes preservation of coseismic deposits sparse. One approach taken by previous researchers is to exploit active fold scarps and related ponded deposits [*Dolan et al*., 2003; *Leon et al*., 2007, 2009]. Because an active FSF can rupture the land surface coseismically to produce a geomorphic scarp with meter-scale height [*Feng*, 1994; *Berberian*, 2014; *Gutiérrez et al*., 2014], at its front, it can preserve considerable deposits that record earthquake events. Compared with the active fold scarps, active FSFs have unique benefits: (i) they are easier to identify and preserve; (ii) much smaller trench lengths and depths are typically needed to expose them, and several individual slip events may be preserved and discernable on the trench walls (Figure 4d); and (iii) the spatial distribution of active FSFs commonly occurs across a broad zone, and if no active fold scarps are present, the study of the active FSFs may be the most viable approach to delimit an earthquake history. Therefore, using a combination of active FSFs and fold scarps may provide a more complete and more accurate paleo-earthquake history.

Nevertheless, the use of FSFs for paleo-earthquake studies should be done cautiously. First, although FSF slip in each event can reach ~1 m [*Feng*, 1994; *Berberian*, 2014; *Gutiérrez et al*., 2014], most studies indicate that such slip is likely to be on an order of several centimeters [*Philip and Meghraoui*, 1983; *Klinger and Rockwell*, 1989; *Walker et al*., 2003, 2013], which makes it challenging to distinguish individual events in a trench. Second, at the Mingyaole fold, FSF scarps closer to the hinge appear to be activated more easily than those farther away from the hinge, but it is unknown whether such faults are active during all events. Therefore, multiple trenches of FSFs closer to the hinge are necessary to reveal a more complete earthquake history. The third point is that some fold growth may be aseismic [*Fielding et al*., 2004; *Copley*, 2014] or be produced during earthquakes in which the major coseismic slip is not accommodated by underlying thrust controlling the fold but accommodated by nearby structures [*Feng*, 1994; *Berberian et al*., 2001]. Hence, it follows that some slip on FSFs can occur by such mechanisms. For example, although some Mingyaole FSFs were displaced in 1985 Wuqia event, the major coseismic slip in this event has not occurred on the main thrust fault underlying the Mingyaole fold but instead occurred on the Pamir Frontal Thrust to its south (Figure 2) [*Feng*, 1994]. Such aseismic slip or coseismic slip accompanied with nearby active structures is likely to be indistinguishable from slip induced by earthquakes in which the major or total coseismic slip occurs on the master fault responsible for creating the overall fold growth. Hence, some caution should be used when reconstructing slip histories for FSFs in an active fold when nearby active structures are present.

6. Conclusions

Numerous, well-exposed suites of flexural-slip faults (FSFs) at the Mingyaole and Wulagen folds in the Pamir-Tian Shan convergent zone permit a new quantification of their typical patterns of displacement, their systematic deformation of geomorphic surfaces, and a geometric modeling of their faulting and geomorphic consequences. Our study reveals well-defined and perhaps characteristic features of active flexural-slip faulting:

1. FSF scarps commonly occur near a synclinal hinge, regardless of whether the dip direction of the beds on either side of hinge is unidirectional or in opposite directions, whether the hinge is migrating or fixed, or whether the hinge shape is narrow and angular or wide and curved.
2. Active FSFs are likely to produce higher scarps when the underlying beds are steeper, whereas lower or no topographic scarps may occur on gentler beds.
3. The height of FSF scarps generally increases on progressively higher, older terrace surfaces, but the number and spatial distribution may be similar.
4. The tilt angle of a terrace surface decreases gradually farther away from the hinge, and abrupt changes of tilt angles typically coincide with the surface traces of FSF scarps. The changes of tilt angle and scarp height have a predictable geometric relationship.

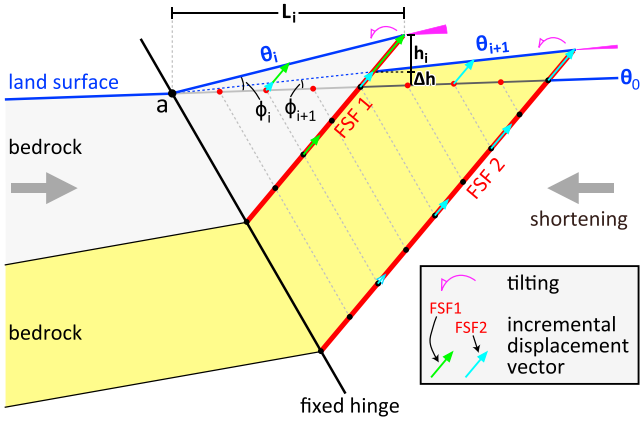

Figure A1. Geometry of active flexural-slip faulting with the fixed angular hinge model in Figure 10b. φ_i and φ_{i+1} are the magnitude of additional tilt angle of the land surface caused by slip on the FSFs.

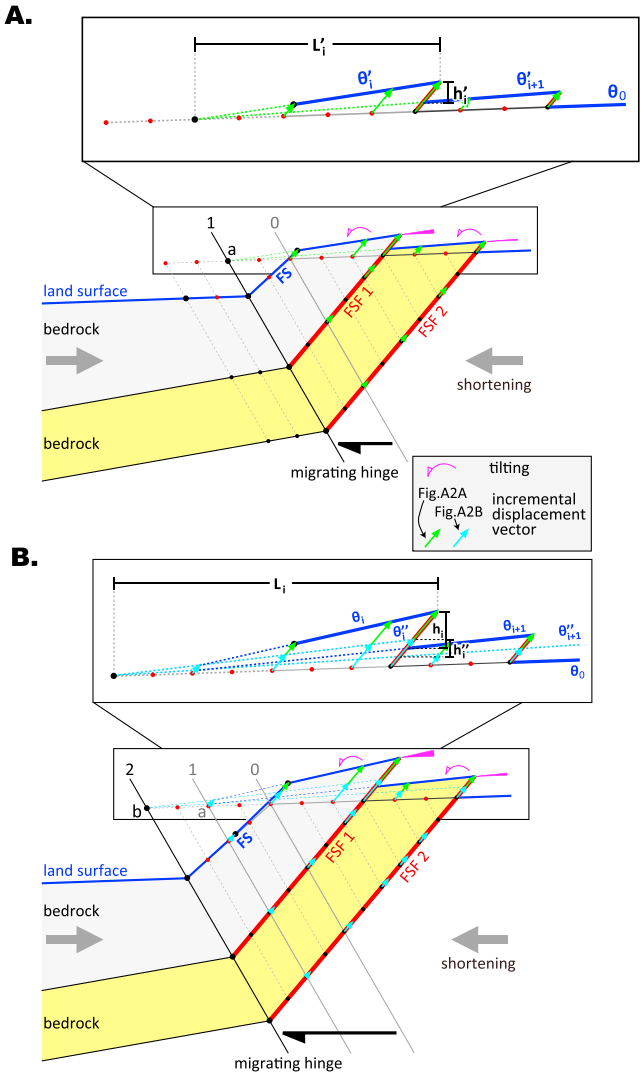

Figure A2. Geometry of active flexural-slip faulting with the *migrating, angular hinge model* in Figures 11b2 and 11c2.

5. Active FSFs can accommodate a significant fraction of the total slip, thereby playing an important role in accommodating fold deformation.
6. Active FSFs can be useful for determining seismic hazards and paleoearthquake histories associated with active blind thrusts.

Despite improved understanding of active flexural-slip faulting, basic questions still await answers. One unresolved issue is the causal linkage of FSF scarps with bed dips. Previous studies [*Ramsay*, 1967; *Johnson and Johnson*, 2000; *Walker et al.*, 2013] and our study indicate that the steeper the underlying beds, the more likely will be the presence of FSF scarps. It is unknown whether a threshold angle exists below which scarps are indiscernible. Other questions concern the paleo-earthquake record that FSF scarps may produce: do they have enough high-resolution data to record the complete history of paleoearthquakes and does a reliable relationship exist between the slip on an individual FSF and the slip of underlying master fault during an earthquake? The answers to these questions will require additional, well-calibrated field studies and analogue models.

Appendix A: Geometry of Active Flexural-Slip Faulting

For the fixed angular hinge model (Figure A1), we have

$$\frac{h_i}{L_i} = \frac{h_i + \Delta h}{L_i} - \frac{\Delta h}{L_i} = \tan\phi_i - \tan\phi_{i+1} \quad \text{(A1)}$$

where ϕ_i and ϕ_{i+1} are the amount of additional tilting caused by faulting of the land surface, L is the horizontal distance from the FSF to the fold hinge, h is the vertical displacement across the fault (FSF1), and Δh equals the displacement due to slip on the subjacent fault (FSF2). Because these two angles are very small (commonly $<15°$), we have $\tan\phi_i \approx \phi_i$ and $\tan\phi_{i+1} \approx \phi_{i+1}$.

Consequently, the formula (A1) can be transformed to

$$\frac{h_i}{L_i} \approx \phi_i - \phi_{i+1} = (\theta_i - \theta_0) - (\theta_{i+1} - \theta_0) = \theta_i - \theta_{i+1} = \Delta\theta \tag{A2}$$

That is,

$$\Delta\theta = \theta_i - \theta_{i+1} \approx \frac{h_i}{L_i} \tag{A3}$$

where θ_0 is the original slope of the land surface and θ_i and θ_{i+1} are the land surface slope after flexural-slip faulting.

For the migrating angular hinge model (Figure A2), we have the same geometric relationship as in the fixed angular hinge model in the first (Figure A2a) and second (Figure A2b) stages:

$$\Delta\theta' = \theta'_i - \theta'_{i+1} \approx \frac{h'_i}{L'_i} \tag{A4}$$

$$\Delta\theta'' = \theta''_i - \theta''_{i+1} \approx \frac{h_i}{L_i} \tag{A5}$$

Adding up formulas (A4) and (A5), we have

$$\Delta\theta' + \Delta\theta'' = (\theta'_i + \theta''_i) - (\theta'_{i+1} + \theta''_{i+1}) \approx \frac{h'_i}{L'_i} + \frac{h''_i}{L_i} \tag{A6}$$

As the hinge migrates, the L''_i is larger than the L'_i. Then we have

$$\Delta\theta' + \Delta\theta'' = (\theta'_i + \theta''_i) - (\theta'_{i+1} + \theta''_{i+1}) > \frac{h'_i}{L_i} + \frac{h''_i}{L_i} = \frac{h'_i + h''_i}{L_i} \tag{A7}$$

That is,

$$\Delta\theta = \theta_i - \theta_{i+1} > \frac{h_i}{L_i} \tag{A8}$$

If the hinge migrates only once, we have

$$\Delta\theta = \theta_i - \theta_{i+1} = \frac{h_i}{L_i} \tag{A9}$$

which is the same geometric relationship as the fixed angular hinge model (formula (A3)). Therefore,

$$\Delta\theta = \theta_i - \theta_{i+1} \geq \frac{h_i}{L_i} \tag{A10}$$

Acknowledgments

Data supporting topographic survey data of flexural-slip fault scarps and fold scarps in Figures 5, 6, and 9 are available in the supporting information. This study was supported by the China NSF (41302172, 41472176, and 41172183), State Key Laboratory of Earthquake Dynamics of China (LED2010A04), and the U.S. NSF (EAR 1050070), National S&T Major Project of China (2011ZX05003-002), and PetroChina Company (2014B0407). We thank W. Xiao for his help in the field work. Critical and thorough reviews of the manuscript by R. Walker, an anonymous reviewer, and Associate Editor significantly improved the current version.

References

Amos, C. B., and D. W. Burbank (2007), Channel width response to differential uplift, *J. Geophys. Res.*, *112*, F02010, doi:10.1029/2006JF000672.

Amos, C. B., D. W. Burbank, D. C. Nobes, and S. Read (2007), Geomorphic constraints on listric thrust faulting: Implications for active deformation in the Mackenzie Basin, South Island, New Zealand, *J. Geophys. Res.*, *112*, B03S11, doi:10.1029/2006JB004291.

Arrowsmith, J. R., and M. R. Strecker (1999), Seismotectonic range-front segmentation and mountain-belt growth in the Pamir-Alai region, Kyrgyzstan (India-Eurasia collision zone), *Geol. Soc. Am. Bull.*, *111*, 1665–1683, doi:10.1130/0016-7606(1999)111<1665:SRFSAM>2.3.CO;2.

Avouac, J.-P., P. Tapponnier, M. Bai, H. You, and G. Wang (1993), Active thrusting and folding along the northern Tien Shan and Late Cenozoic rotation of the Tarim relative to Dzungaria and Kazakhstan, *J. Geophys. Res.*, *98*(B4), 6755–6804, doi:10.1029/92JB01963.

Berberian, M. (2014), Chapter 15—Coseismic, blind, reverse-fault-related, flexural-slip folding and faulting at the surface, *Dev. Earth Surf. Process.*, *17*, 421–437.

Berberian, M., J. A. Jackson, E. J. Fielding, B. A. Parsons, K. Priestley, M. Qorashi, M. Talebian, R. Walker, T. J. Wright, and C. Baker (2001), The 1998 March 14 Fandoqa earthquake (M_w6.6) in Kerman province, southeast Iran: Re-rupture of the 1981 Sirch earthquake fault, triggering of slip on adjacent thrusts and the active tectonics of the Gowk fault zone, *Geophys. J. Int.*, *146*, 371–398.

Bosboom, R., et al. (2010), Late Eocene sea retreat from the Tarim Basin (west China) and concomitant Asian paleoenvironment change, *Palaeogeogr. Palaeoclimatol. Palaeoecol.*, *299*, 385–398, doi:10.1016/j.palaeo.2010.11.019.

Burbank, D. W., and R. S. Anderson (2011), *Tectonic Geomorphology*, Wiley-Blackwell, West Sussex, U. K.

Burtman, V. S., and P. Molnar (1993), Geological and geophysical evidence for deep subduction of continental crust beneath the Pamir, *Spec. Pap. Geol. Soc. Am.*, *281*, 1–76, doi:10.1130/SPE281-p1.

Chen, J., D. W. Burbank, K. M. Scharer, E. Sobel, J. Yin, C. Rubin, and R. Zhao (2002), Magnetochronology of the Upper Cenozoic strata in the Southern Chinese Tian Shan: Rates of Pleistocene folding and thrusting, *Earth Planet. Sci. Lett.*, *195*, 113–130.

Chen, J., K. M. Scharer, D. W. Burbank, R. Heermance, and C. S. Wang (2005), Quaternary detachment folding of the Mingyaole anticline, southern Tian Shan [in Chinese], *Seismol. Geol.*, *27*, 530–547.

Chen, J., R. Heermance, D. W. Burbank, K. M. Scharer, J. Miao, and C. S. Wang (2007a), Quantification of growth and lateral propagation of the Kashi anticline, southwest Chinese Tian Shan, *J. Geophys. Res.*, *112*, B03S16, doi:10.1029/2006JB004345.

Chen, Y. G., K. Lai, Y. Lee, J. Suppe, W. Chen, Y. Liu, Y. Wang, J. Huang, and Y. Kuo (2007b), Coseismic fold scarps and their kinematic behavior in the 1999 Chi-Chi earthquake Taiwan, *J. Geophys. Res.*, *112*, B03S02, doi:10.1029/2006JB004388.

Copley, A. (2014), Postseismic afterslip 30 years after the 1978 Tabas-e-Golshan (Iran) earthquake: Observations and implications for the geological evolution of thrust belts, *Geophys. J. Int.*, doi:10.1093/gji/ggu023.

Cowgill, E. (2010), Cenozoic right-slip faulting along the eastern margin of the Pamir salient, northwestern China, *Geol. Soc. Am. Bull.*, *122*, 145–161, doi:10.1130/B26520.1.

Dolan, J. F., S. A. Christofferson, and J. H. Shaw (2003), Recognition of paleoearthquakes on the Puente Hills blind thrust fault, California, *Science*, *300*, 115–118.

Feng, X. Y. (1994), Surface rupture associated with the 1985 Wuqia earthquake, in *Xinjiang, Research on Active Fault (3)* [in Chinese], pp. 45–55, Seismological Press, Beijing.

Fielding, E., T. Wright, J. Muller, B. Parsons, and R. Walker (2004), Aseismic deformation of a fold-and-thrust belt imaged by synthetic aperture radar interferometry near Shahdad, southeast Iran, *Geology*, *32*(7), 577–580, doi:10.1130/G20452.1.

Goode, J. K., and D. W. Burbank (2011), The temporal evolution of minor channels on growing folds and its bearing on fold kinematics, *J. Geophys. Res.*, *116*, B04407, doi:10.1029/2010JB007617.

Gutiérrez, F., D. Carbonel, R. M. Mirkeham, J. Guerrero, P. Lucha, and V. Matthews (2014), Can flexural-slip faults related to evaporate dissolution generate hazardous earthquakes? The case of the Grand Hogback monocline of west-central Colorado, *Geol. Soc. Am. Bull.*, doi:10.1130/B31054.1.

Heermance, R. V., J. Chen, D. W. Burbank, and J. J. Miao (2008), Temporal constraints and pulsed Late Cenozoic deformation during the structural disruption of the active Kashi foreland, northwest China, *Tectonics*, *27*, TC6012, doi:10.1029/2007TC002226.

Hubert-Ferrari, A., J. Suppe, R. Gonzalez-Mieres, and X. Wang (2007), Mechanisms of active folding of the landscape (southern Tian Shan, China), *J. Geophys. Res.*, *112*, B03S09, doi:10.1029/2006JB004362.

Ischuk, A., et al. (2013), Kinematics of the Pamir and Hindu Kush regions from GPS geodesy, *J. Geophys. Res. Solid Earth*, *118*, 2408–2416, doi:10.1002/jgrb.50185.

Ishiyama, T., K. Mueller, M. Togo, A. Okada, and K. Takemura (2004), Geomorphology, kinematic history, and earthquake behavior of the active Kuwana wedge thrust anticline, central Japan, *J. Geophys. Res.*, *109*, B12408, doi:10.1029/2003JB002547.

Ishiyama, T., K. Mueller, H. Sato, and M. Togo (2007), Coseismic fault-related fold model, growth structure, and the historic multisegment blind thrust earthquake on the basement-involved Yoro thrust, central Japan, *J. Geophys. Res.*, *112*, B03S07, doi:10.1029/2006JB004377.

Ismat, Z., and G. Mitra (2005a), Fold-thrust belt evolution expressed in an internal thrust sheet, Sevier orogen: The role of cataclastic flow, *Geol. Soc. Am. Bull.*, *117*, 764–782.

Ismat, Z., and G. Mitra (2005b), Folding by cataclastic flow: Evolution of controlling factors during deformation, *J. Struct. Geol.*, *27*, 2181–2203, doi:10.1016/j.jsg.2005.08.005.

Johnson, K. M., and A. M. Johnson (2000), Localization of layer-parallel faults in San Rafael swell, Utah and other monoclinal folds, *J. Struct. Geol.*, *22*, 1455–1468.

Kelsey, H. M., B. L. Sherrod, A. R. Nelson, and T. M. Brocher (2008), Earthquakes generated from bedding plane-parallel reverse faults above an active wedge thrust, Seattle fault zone, *Geol. Soc. Am. Bull.*, *120*, 1581–1597.

Kirby, E., and K. X. Whipple (2012), Expression of active tectonics in erosional landscapes, *J. Struct. Geol.*, *44*, 57–75.

Klinger, R. E., and T. K. Rockwell (1989), Flexural-slip folding along the eastern Elmore Ranch fault in the Superstition Hills earthquake sequence of November 1987, *Bull. Seismol. Soc. Am.*, *79*(2), 297–303.

Lavé, J., and J. P. Avouac (2000), Active folding of fluvial terraces across the Siwaliks Hills, Himalayas of central Nepal, *J. Geophys. Res.*, *105*(3), 5735–5770, doi:10.1029/1999JB900292.

Leon, L. A., S. A. Christofferson, J. F. Dolan, J. H. Shaw, and T. L. Pratt (2007), Earthquake-by-earthquake fold growth above the Puente Hills blind thrust fault, Los Angeles, California: Implications for fold kinematics and seismic hazard, *J. Geophys. Res.*, *112*, B03S03, doi:10.1029/2006JB004461.

Leon, L. A., J. F. Dolan, J. H. Shaw, and T. L. Pratt (2009), Evidence for large Holocene earthquakes on the Compton thrust fault, Los Angeles, California, *J. Geophys. Res.*, *114*, B12305, doi:10.1029/2008JB006129.

Li, T., J. Chen, W. P. Xiao, D. W. Burbank, J. A. Thompson, and X. Yang (2011), The discovery and geologic significance of the thrust at south limb of the Wulagen Anticline, south margin of the southwestern Tian Shan [in Chinese], *Seismol. Geol.*, *33*(2), 277–288.

Li, T., J. Chen, J. A. Thompson, D. W. Burbank, and W. P. Xiao (2012), Equivalency of geologic and geodetic rates in contractional orogens: New insights from the Pamir Frontal Thrust, *Geophys. Res. Lett.*, *39*, L15305, doi:10.1029/2012GL051782.

Li, T., J. Chen, J. A. Thompson, D. W. Burbank, and X. Yang (2013a), Quantification of three-dimensional folding using fluvial terraces: A case study from the Mushi anticline, northern margin of the Chinese Pamir, *J. Geophys. Res. Solid Earth*, *112*, B03S09, doi:10.1029/2006JB004362.

Li, T., J. Chen, and W. P. Xiao (2013b), Late-Quaternary folding of the Mingyaole Anticline southwestern tip, Pamir-Tianshan convergent zone [in Chinese], *Seismol. Geol.*, *35*(2), 234–246.

Li, T., J. Chen, and W. P. Xiao (2014), Deformation characteristics and kinematics of active detachment fold scarp: A case study from the Mingyaole Anticline, Pamir-Southern Tian Shan foreland [in Chinese], *Seismol. Geol.*, *36*(3), 677–691.

Mitra, S. (2002), Structural models of faulted detachment folds, *AAPG Bull.*, *86*, 1673–1694.

Molnar, P., et al. (1994), Quaternary climate change and the formation of river terraces across growing anticlines on the north flank of the Tien Shan, China, *J. Geol.*, *102*(5), 583–602.

Negredo, A., A. Replumaz, A. Villaseñor, and S. Guillot (2007), Modeling the evolution of continental subduction processes in the Pamir-Hindu Kush region, *Earth Planet. Sci. Lett.*, *259*(1–2), 212–225, doi:10.1016/j.epsl.2007.04.043.

Niño, F., H. Philip, and J. Chery (1998), The role of bed-parallel slip in the formation of blind thrust faults, *J. Struct. Geol.*, *20*(5), 503–516.

Philip, H., and M. Meghraoui (1983), Structural analysis and interpretation of the surface deformations of the El Asnam earthquake of October 10, 1980, *Tectonics*, *2*, 17–50, doi:10.1029/TC002i001p00017.

Poblet, J., and K. McClay (1996), Geometry and kinematics of single-layer detachment folds, *AAPG Bull.*, *80*(7), 1085–1109.

Ramsay, J. G. (1967), *Folding and Fracturing of Rocks*, McGrawHill, New York.

Reigber, C., G. W. Michel, R. Galas, D. Angermann, J. Klotz, J. Y. Chen, A. Papschev, R. Arslanov, V. E. Tzurkov, and M. C. Ishanov (2001), New space geodetic constraints on the distribution of deformation in Central Asia, *Earth Planet. Sci. Lett.*, *191*, 157–165, doi:10.1016/S0012-821X(01)00414-9.

Rockwell, T. K., E. A. Keller, and M. N. Clark (1984), Chronology and rates of faulting of Ventura River terraces, California, *Geol. Soc. Am. Bull.*, *95*, 1466–1474.

Rockwell, T. K., E. A. Keller, and G. R. Dembrof (1988), Quaternary rate of folding of the Ventura Avenue anticline, western Transverse Ranges, southern California, *Geol. Soc. Am. Bull.*, *100*, 850–858.
Roering, J. J., M. L. Cooke, and D. D. Pollard (1997), Why blind thrust faults do not propagate to the Earth's surface: Numerical modeling of coseismic deformation associated with thrust-related anticlines, *J. Geophys. Res.*, *102*, 11,901–11,912, doi:10.1029/97JB00680.
Sanz, P. F., D. D. Pollard, P. F. Allwardt, and R. I. Borja (2008), Mechanical models of fracture reactivation and slip on bedding surfaces during folding of the asymmetric anticline at Sheep Mountain, Wyoming, *J. Struct. Geol.*, *30*(9), 1177–1191.
Scharer, K. M., D. W. Burbank, J. Chen, R. J. Weldon, C. Rubin, R. Zhao, and J. Shen (2004), Detachment folding in the Southwestern Tian Shan-Tarim foreland, China: Shortening estimates and rates, *J. Struct. Geol.*, *26*, 2119–2137.
Scharer, K. M., D. W. Burbank, J. Chen, and R. J. Weldon II (2006), Kinematic models of fluvial terraces over active detachment fold: Constraints on the growth mechanism of the Kashi-Atushi fold system, Chinese Tian Shan, *Geol. Soc. Am. Bull.*, *118*, 1006–1021, doi:10.1130/B25835.1.
Schneider, F. M., et al. (2013), Seismic imaging of subducting continental lower crust beneath the Pamir, *Earth Planet. Sci. Lett.*, *375*, 101–112.
Shaw, J., and J. Suppe (1994), Active faulting and growth folding in the eastern Santa Barbara Channel, California, *Geol. Soc. Am. Bull.*, *106*, 607–626.
Sippl, C., et al. (2013), Geometry of the Pamir-Hindu Kush intermediate-depth earthquake zone from local seismic data, *Earth Planet. Sci. Lett.*, *118*, 1–20, doi:10.1002/jgrb.50128.
Sobel, E. R., and T. A. Dumitru (1997), Thrusting and exhumation around the margins of the western Tarim Basin during the India-Asia collision, *J. Geophys. Res.*, *102*(B3), 5043–5063, doi:10.1029/96JB03267.
Sobel, E. R., J. Chen, and R. V. Heermance (2006), Late Oligocene-Early Miocene initiation of shortening in the southwestern Chinese Tian Shan: Implications for Neogene shortening rate variations, *Earth Planet. Sci. Lett.*, *247*, 70–81, doi:10.1016/j.epsl.2006.03.048.
Sobel, E. R., L. M. Schoenbohm, J. Chen, R. Thiede, D. F. Stockli, M. Sudo, and M. Strecker (2011), Late Miocene-Pliocene deceleration of dextral slip between Pamir and Tarim: Implications for Pamir orogenesis, *Earth Planet. Sci. Lett.*, *304*, 369–378, doi:10.1016/j.epsl.2011.02.012.
Sobel, E. R., J. Chen, L. M. Schoenbohm, R. Thiede, D. F. Stockli, M. Sudo, and M. Strecker (2013), Oceanic-style subduction controls late Cenozoic deformation of the Northern Pamir orogen, *Earth Planet. Sci. Lett.*, *363*, 204–218.
Suppe, J., G. T. Chou, and S. C. Hook (1992), Rates of folding and faulting determined from growth strata, in *Thrust Tectonics*, edited by K. R. McClay, pp. 105–121, CRC Press, Boca Raton, Fla.
Suppe, J., F. Sabat, J. A. Munoz, J. Poblet, E. Roca, and J. Verges (1997), Bed-by-bed fold growth by kink-band migration: Sant Llorenc de Morunys, eastern Pyrenees, *J. Stru. Geol.*, *19*(3–4), 443–461, doi:10.1016/S0191-8141(96)00103-4.
Suppe, J., C. Connors, and Y. Zhang (2004), Shear fault-bend folding, *AAPG Mem.*, *82*, 303–323.
Tanner, P. (1989), The flexural-slip mechanism, *J. Struct. Geol.*, *11*(6), 635–655.
Thompson, J. A. (2013), Neogene tectonic evolution of the NE Pamir margin, NW China, UC Santa Barbara PhD thesis, Part III, 68–138.
Thompson, S. C., R. J. Weldon, C. M. Rubin, K. Abdrakhmatov, P. Molnar, and G. W. Berger (2002), Late Quaternary slip rates across the central Tien Shan, Kyrgyzstan, central Asia, *J. Geophys. Res.*, *107*(B9), 2203, doi:10.1029/2001JB000596.
Walker, R., J. Jackson, and C. Baker (2003), Surface expression of thrust faulting in eastern Iran: Source parameter and surface deformation of the 1978 Tabas and 1968 Ferdows earthquake sequences, *Geophys. J. Int.*, *152*, 749–765.
Walker, R., M. Khatib, A. Bahroudi, A. Rodés, C. Schnabel, M. Fattahi, M. Talebian, and E. Bergman (2013), Co-seismic, geomorphic, and geologic fold growth associated with the 1978 Tabas-e-Golshan earthquake fault in eastern Iran, *Geomorphology*, doi:10.1016/j.geomorph.2013.02.016.
Wei, H. H., Q. Meng, L. Ding, and Z. Li (2013), Tertiary evolution of the western Tarim Basin, northwest China: A tectono-sedimentary response to northward indentation of the Pamir salient, *Tectonics*, *32*, 558–575, doi:10.1002/tect.20046.
Yang, S. M., J. Li, and Q. Wang (2008), The deformation pattern and fault rate in the Tianshan Mountains inferred from GPS observations, *Sci. China, Ser. D*, *51*(8), 1064–1080, doi:10.1007/s11430-008-0090-8.
Yang, X. D., J. Chen, T. Li, W. Li, L. Liu, and H. Yang (2014), Active folding and active flexural-slip fault scarps on Mingyaole anticline, west margin of Tarim [in Chinese], *Seismol. Geol.*, *36*(1), 14–27.
Yeats, R. S., M. N. Clark, E. A. Keller, and T. K. Rockwell (1981), Active fault hazard in south California: Ground rupture versus seismic shaking, *Geol. Soc. Am. Bull.*, *92*, 189–196.
Yeats, R. S., K. S. Sieh, and C. R. Allen (1997), *Geology of Earthquake*, pp. 344–346, Oxford Univ. Press, New York.
Yin, A., S. Nie, P. Craig, T. M. Harrison, F. J. Ryerson, X. Qian, and G. Yang (1998), Late Cenozoic tectonic evolution of the southern Chinese Tian Shan, *Tectonics*, *17*(1), 1–27, doi:10.1029/97TC03140.
Yin, A., et al. (2002), Tectonic history of the Altyn Tagh fault system in northern Tibet inferred from Cenozoic sedimentation, *Geol. Soc. Am. Bull.*, *114*, 1257–1295, doi:10.1130/0016-7606.
Zubovich, A. V., et al. (2010), GPS velocity field of the Tien Shan and surrounding regions, *Tectonics*, *29*, TC6014, doi:10.1029/2010TC002772.